



# Assessing the feasibility of laser induced breakdown spectroscopy for detecting nitrogen in martian surface sediments

Erin F. Gibbons<sup>\*</sup>, Richard Léveillé<sup>1</sup>, Kim Berlo<sup>1</sup>

Geotop, Department of Earth and Planetary Sciences, McGill University, 3450 University Street, Montreal, Quebec H3A 0E8, Canada

## ARTICLE INFO

### Keywords:

Laser-induced breakdown spectroscopy  
Mars  
Astrobiology  
Nitrogen  
Nitrate

## ABSTRACT

Despite the detection of fixed nitrogen in meteorites and directly on Mars' surface, the abundance and distribution of nitrogen sequestered in the martian crust remains unknown. Given that nitrogen is a bioessential element that is required for the synthesis of amino acids, nucleic acids, and other organic molecules vital for life, this gap in knowledge is one of the most important challenges in constraining martian habitability. Laser-induced breakdown spectroscopy (LIBS) has the capability to detect N in natural rock samples and is available as a stand-off survey instrument on multiple currently active Mars rovers, creating an immediate opportunity to map the stratigraphic distribution of N within diverse depositional settings. However, little has been published regarding the detection of N with LIBS.

To lay a foundation for N detection on Mars using LIBS, we synthesized a comprehensive suite of samples with variable amounts of nitrogen (as nitrate or ammonium) in either a Mars regolith simulant or a clay matrix. We present baseline spectra of N emission in Mars-relevant matrices and identify spectral interferences. Our results indicate that 17 diagnostic N emission lines are reliably detectable from mineral-bound N against a basaltic background, but only four lines exhibit sufficient sensitivity to be detected across a range of N concentrations and within all tested matrices. To elucidate optimized strategies for quantification, we present an iterative series of PLS models. We find that prediction accuracy is improved by restricting the compositional range of the training set, normalizing the data, subtracting baseline continuum emission, and simultaneously modeling the emission behaviour of multiple diagnostic N lines at once. We observe that the prediction uncertainty increases (worsens) from 8.4% to 29.9% if models are used to predict N in samples with a dissimilar matrix than those used during training, suggesting poor generalizability outside the training range. Consequently, future work should focus on developing a larger, more diverse training set that encompasses the range of N concentrations and phases expected to be encountered on Mars, which may be used to train generalizable models. Overall, this work demonstrates that LIBS is a promising tool for determining the abundance of N sequestered in martian surface materials and lays a foundation for future development.

## 1. Introduction

The search for evidence of habitable conditions and signs of life, extinct or extant, on Mars is now a primary objective for space agencies [1–3]. While previous missions have shown that Mars met many of the requirements for life throughout its history, at least episodically (e.g., [1]), our knowledge of Mars' bioavailable (or "fixed") nitrogen, N, stores remains limited [4,5]. Terrestrial life requires fixed forms of N for synthesizing essential biomolecules such as amino acids and nucleotides, which serve as the building blocks for DNA, RNA, and proteins [6].

Additionally, N atoms are a key functional component in ATP, co-enzymes, vitamins, and pigments, thus playing a vital role in information storage, enzymatic activity, and metabolism in all known organisms [6]. Indeed, in terrestrial ecosystems, N is often a limiting nutrient that exerts a principal control over biomass and biodiversity [7]. Therefore, determining the amount and distribution of fixed forms of N sequestered in Mars' crust is a crucial outstanding factor in constraining martian habitability [5,8] and could help direct current and future missions towards areas with the greatest astrobiological potential.

Experimental studies have demonstrated that natural, abiotic N

<sup>\*</sup> Corresponding author.

E-mail address: [erin.gibbons@mail.mcgill.ca](mailto:erin.gibbons@mail.mcgill.ca) (E.F. Gibbons).

<sup>1</sup> These authors contributed equally to this work.

fixation processes (i.e., the conversion of  $N_2$  into biologically available nitrogenous compounds) are plausible on Mars [9,10]. Nitrate ions,  $NO_3^-$ , are predicted to be the predominant end product of such processes, capable of forming soluble salts with the cationic components released during the weathering of martian basalts, such as  $Na^+$ ,  $K^+$ ,  $Mg^{2+}$ ,  $Ca^{2+}$ ,  $Fe^{2+}$  or  $3^+$  [5]. These salts are expected to undergo burial in the regolith and subsequent incorporation into sedimentary rocks, ultimately becoming stored in the top layers of the martian lithosphere [5]; Manning et al. [11] calculated a putative nitrate reservoir of  $\sim 5 \times 10^{18}$  mol on Mars. Ammonium ions,  $NH_4^+$ , are also plausible end products of martian N fixation when ferrous iron is available [5,12]. Ammonium ions could then be adsorbed as an exchangeable ion or be mineralogically fixed in the crystal lattice of certain phyllosilicate minerals [13,14]. Importantly, with a largely non-recycled crust, both of these thermodynamically stable end products of N fixation are hypothesized to accumulate and persist in Mars' surface/shallow subsurface as a stable reservoir of fixed N [5].

Detections of putative  $NO_3^-$  in Martian meteorites [15,16] and sedimentary deposits of Gale Crater, as observed by the Sample Analysis at Mars (SAM) instrument [17], corroborate these predictions. However, meteorites lack a clear geological context, and although the SAM instrument has successfully detected fixed N phases in situ, its analyses are confined to a relatively small area. Additionally, the frequency of SAM analyses is constrained by the time and costs of each analysis, as well as the need to balance them with other science activities of the *Mars Science Laboratory*. The available data on Mars' fixed N species are thus insufficient to comprehensively understand either the stratigraphic distribution of fixed N or the underlying processes governing its distribution. Consequently, the size and extent of Mars' fixed N reservoir remain largely unknown. Furthermore, efforts to detect fixed N compounds from orbit have been unsuccessful to date, possibly because their concentrations fall below the detection limit of current orbiters or due to interference from dust [18,19]. There is therefore a need for rapid and frequent in situ N measurements to advance our understanding of the stratigraphic distribution of sequestered N phases.

We explore the capacity for laser-induced breakdown spectroscopy (LIBS) to meet this need. At the time of writing, LIBS technology has been included on the payloads of the three most recent Mars rovers: NASA's *Curiosity* and *Perseverance* rovers, and the China National Space Administration's *Zhùróng* rover. These rovers are exploring separate regions of Mars, each with a unique geological context. The two NASA LIBS instruments (ChemCam and SuperCam) are used frequently as chemical surveyors and have proven highly effective in generating a near-continuous record of geochemical data throughout the rovers' traverses [20,21]. Therefore, by enabling accurate N detection and quantification with LIBS technology, we could immediately begin to map the N stored within distinct martian depositional environments at high spatial resolution.

However, three significant factors challenge N detection with this technique and very little has thus been published on the nature of LIBS N emission, especially from inorganic fixed N sources. First, N has a high ionization potential (first ionization energy = 14.5 eV), resulting in generally weak emission lines in a LIBS spectrum [22]. This becomes problematic when N occurs in a matrix that also contains elements with lower ionization energies—such as alkalis, alkaline earth elements, and transition metals—which produce more intense emission lines. Second, the strongest N emission lines are found in the vacuum ultraviolet region (30–200 nm) [22], which lie outside of the operational range of most commercial LIBS detectors, as well as those on the Mars rovers. LIBS N detection is therefore often limited to the comparatively weaker emission lines accessible in the longer wavelength ultraviolet to infrared regions, which hinders identification. Lastly, the use of LIBS for routine N analyses on Earth is challenged by interference from our  $N_2$ -rich atmosphere (>78% by volume). As a result, it is difficult to disambiguate contributions from the sample and the atmosphere, which has limited the overall depth and breadth of research on LIBS N emission

characteristics [23]. Preliminary work by Dequaire et al. (2017) [24], however, suggests that the much lower  $N_2$  content in Mars' atmosphere (only  $\sim 2.6\%$   $N_2$  (g) by volume) has a negligible effect on LIBS N emission from geological samples.

Considering these challenges and the dearth of systematic studies for optimizing N detection with LIBS, we undertook a focused investigation designed to:

1. Establish a baseline understanding of the LIBS N spectrum, with consideration of potentially interfering emission lines from other rock-forming elements expected to coexist in natural N-bearing materials on Mars.
2. Elucidate the optimal strategies for reliable detections and quantification.

The ultimate goal of this work is to lay the foundation for the use of remote LIBS for N analyses in planetary exploration so that astrobiologically important N stores may be discovered, explored, and possibly prioritized for sample return.

## 2. Methods and rationale

### 2.1. Sample synthesis

On Mars, abiotic  $N_2$  (g) fixation is expected to result in two primary N sinks: nitrate salts and ammoniated phyllosilicates [5]. We synthesized two distinct sample suites to simulate both possible outcomes.

#### 2.1.1. Nitrate salt sample suite

To investigate the potential for LIBS to identify  $NO_3^-$ -derived N in Mars' sedimentary deposits, we created a series of mixtures containing decreasing proportions of various nitrate salts dispersed in a basaltic matrix. For the salt phases, we purchased high-purity nitrate salts complexed to cations known to be abundant on the martian surface:  $NaNO_3$ ,  $KNO_3$ ,  $Mg(NO_3)_2$ ,  $Ca(NO_3)_2$ , and  $Fe(NO_3)_3$ . For the matrix, we use the Mars Global Simulant (MGS-1) from the Exolith Lab [35], a high-fidelity basalt soil standard developed based on quantitative mineralogy from the Mars Science Laboratory (MSL) *Curiosity* rover [25]. The product details of the purchased salts and the bulk chemical and mineralogical properties of MGS-1 are summarized in Tables S1–S3.

To facilitate homogenous mixing and enable pellet pressing without the use of a binding agent, the particle sizes of the salts and MGS-1 powder were reduced as follows. An aliquot of each salt was first placed in a vacuum desiccator for 24 h to reduce clumping and gently crushed using an agate mortar and pestle; the MGS-1 powder was ground in a planetary ball mill to  $<1 \mu m$ . Predetermined amounts of each salt were then weighed on a four-decimal-point scale and separately mixed with MGS-1, creating a sample series with increasing proportions of each salt. Mixture ratios were calculated to produce samples with 0.5, 5, 10, 15, 25, and 30 wt% of the  $NO_3^-$  ion. We specifically calculated the mixing ratios according to the quantity of the  $NO_3^-$  ion to ensure that the molecular fraction of N was identical across each series, regardless of the stoichiometric content of N in each salt. The lowest concentration of 0.5 wt%  $NO_3^-$  is commensurate with the quantity of  $NO_3^-$  identified in the Mars meteorite EETA79001 [15], while the higher concentrations reflect the range of  $NO_3^-$  observed in the Atacama Desert [26], a high-fidelity terrestrial analogue site for investigating Mars' nitrate deposits [5,27]. We followed the mixing procedure described by Chen et al. (2019) [28] for the preparation of homogeneously spiked soils.

Finally, the mixed samples were pressed into 13 mm diameter pellets using an estimated pressure of  $2 \times 10^6$  Pa (uncorrected for friction) for two minutes (a procedure previously validated in our lab to produce robust pellets for LIBS analysis without binding agents [29]). A portion of MGS-1 powder, and an aliquot of each pure salt powder, were also pressed into pellets using the same procedure to represent the end-

members of each dilution series.

Table 1 summarizes the full nitrate salt sample suite. The total N content of the end-member samples and a subset of the mixture samples (5 and 30 wt% mixtures) was verified externally by Activation Laboratories Ltd. using a Leco CNS-2000 Analyzer. The measured N values match the concentrations based on the relative weights with a mean percentage error of 5.2% (details provided in section S2).

### 2.1.2. Ammoniated clay sample suite

To investigate the potential for LIBS to identify  $\text{NH}_4^+$ -derived N, we considered the possible modes of  $\text{NH}_4^+$  sequestration. On Mars, otherwise labile  $\text{NH}_4^+$  ions could be stabilized by phyllosilicate minerals via adsorption to the mineral surface or by penetrating into the interlayer of 2:1 minerals as an exchangeable cation and subsequently becoming chemically bound [5,13]. To assess both these pathways, we saturated various Mars-relevant clays with a solution of  $\text{NH}_4^+$ , then leached them to remove all but the chemically bound  $\text{NH}_4^+$  ions.

We chose to focus our investigation on 2:1 clay minerals, as these are the most effective phyllosilicates for storing  $\text{NH}_4^+$  ions [14]. The most commonly identified 2:1 clay minerals on Mars are Fe/Mg-smectites (e.g., nontronites) and Al-smectites (e.g., montmorillonites) [30] and are therefore the subject of our investigation. We purchased two nontronite samples, NAu-1 and NAu-2, and two montmorillonite samples, SAz-1 and SWy-3, from the Clay Mineral Society. The bulk chemical and mineralogical properties of these samples are summarized in Table S2 and Table S3 (Appendix), respectively. The clays were gently crushed in an agate mortar and pestle to permit better pellet cohesion.

To ammoniate the clays, separate aliquots of each sample were suspended in 1 M  $\text{NH}_4$ -acetate solution at a ratio of 10 parts solution to 1

**Table 1**

Summary of nitrate sample suite. Predetermined amounts of each salt were weighed and separately mixed with MGS-1 to yield 5 salt dilution series, each containing samples with 0.5, 5, 10, 15, 25, and 30 wt% of the  $\text{NO}_3^-$  ion. The corresponding wt% of N, based on the weighing procedure is listed.

Nitrate Salt	Doping Condition of $\text{NO}_3^-$ ion	Corresponding N (wt%)
$\text{Fe}(\text{NO}_3)_3$	0.5	0.11
	5	1.13
	10	2.26
	15	3.39
	25	5.65
	30	6.78
	100 (pure salt)	10.40
	0.5	0.11
	5	1.13
	10	2.26
	15	3.39
	25	5.65
	30	6.78
	100 (pure salt)	11.86
	0.5	0.11
$\text{Ca}(\text{NO}_3)_2$	5	1.13
	10	2.26
	15	3.39
	25	5.65
	30	6.78
	100 (pure salt)	10.93
	0.5	0.11
	5	1.13
	10	2.27
	15	3.39
	25	5.65
	30	6.78
	100 (pure salt)	16.48
	0.5	0.11
	5	1.13
$\text{NaNO}_3$	10	2.26
	15	3.39
	25	5.65
	30	6.78
	100 (pure salt)	13.85

part mineral powder (vol./wt.) (an excess solution volume is required to accommodate for the swelling of the clay mineral). The mixture was agitated on a shaker table at 500 rpm for 1.5 h to ensure complete saturation and then allowed to settle for 72 h at room temperature. After settling, the majority of the  $\text{NH}_4$ -acetate supernatant was removed via pipetting. Half of slurry was removed, dried at 40 °C for 24 h, and lightly disaggregated in a mortar and pestle. This aliquot was designated the “saturated” condition and represents clays with both surface-adsorbed and interlayer  $\text{NH}_4^+$  ions. The other half of the slurry was leached according to the methods described by Bishop et al. [13]. In brief, these slurries were suspended in excess de-ionized water (10:1 vol./wt.), shaken to dissolve the surficially adsorbed salts, and centrifuged at 9000 rpm for 25 min to concentrate the clay particles. The liquid supernatant was removed by pipetting and the leaching treatment was repeated twice more. Finally, the leached slurries were dried and lightly disaggregated. These samples were designated as the “leached” condition and represent clays with primarily the interlayer  $\text{NH}_4^+$  ions remaining.

Powders from the “saturated” and “leached” treatments were pressed into pellets using the same protocol described for the nitrate samples. The ammoniated clay sample suite is summarized in Table 2. As above, the total N content of each sample was measured externally by Activation Laboratories Ltd. using a Leco CNS-2000 Analyzer.

### 2.2. LIBS measurements

LIBS spectra were collected at McGill University using a J200 instrument (Applied Spectra, Fremont, CA, USA) controlled by the Axiom 2.0 software. This system consists of a 213 nm nanosecond Nd:YAG laser with a pulse width of <5 ns, a repetition rate 10 Hz, and a maximum power output of 100 mJ. The six-channel spectrometer is fitted with gated CCD arrays for instant whole spectrum registration in the 186–1042 nm range at a resolution of  $\approx 0.07$  nm. The sealed ablation chamber features an xyz translational stage, a full-colour camera for focus and targeting, and the option to supply gases during the course of the experiment.

To remove interference from atmospheric  $\text{N}_2$  (g), the sample chamber was purged of air before each analysis and flushed with Helium (He) for 4.5 min. Samples were allowed to sit in the He atmosphere for at least 30 min prior to analysis.

Before beginning data collection, the adjustable instrument parameters were systematically varied to optimize the peak-to-base ratio of the N(I) line at 746.8 nm. The 746.8 nm line was used as an initial reference because it has a high relative intensity (compared to other N emission lines) [31], has only a small number of potential spectral interferences, and has previously been reported as a reliable emission feature from inorganic N sources [22]. Optimal parameters were: a delay time of 0.15  $\mu\text{s}$  (the gate width is fixed at 1.05  $\mu\text{s}$ ), a laser power of 1.5 mJ/pulse, and a spot size of 25  $\mu\text{m}$  diameter. These parameters produced a laser fluence of  $\approx 611$  mJ/cm<sup>2</sup>.

Using these parameters, 100 consecutive laser pulses were fired in a line pattern on each sample surface; their data were accumulated into a single spectrum. A linear scan was used to expose a new portion of the

**Table 2**

Summary of ammoniated clay sample suite. The  $\text{NH}_4^+$  ion was introduced to four Mars-relevant clays using 1 M  $\text{NH}_4$ -acetate solution. N content was verified by Activation Laboratories Ltd. (see text for details).

Clay Matrix	Saturation Condition	N (wt%)
NAu-1	Leached	1.34
	Saturated	1.99
NAu-2	Leached	1.01
	Saturated	1.59
SAz-1	Leached	1.61
	Saturated	2.26
SWy-3	Leached	0.95
	Saturated	1.83

sample surface for each acquisition, ensuring that the final accumulated spectrum represented an average bulk chemical fingerprint and accounted for any small heterogeneities that may have persisted through the sample synthesis process. This acquisition procedure was repeated for a total of five (non-overlapping) line scans per sample, producing five accumulated spectra per sample. For the calibration exercises described in section 4.1.2, the five spectra from each pellet were averaged to provide one representative spectrum for each sample with which to model. All spectra were acquired within 7 days.

### 2.3. Spectral identification

Visualization of the LIBS spectra and line identification was carried out using version 18.0.1.34 of the built-in Clarity Software (Applied Spectra) of the LIBS instrument. Emission features that are diagnostic of the presence of N were initially identified within the samples by regressing the known quantity of N in each sample against the 12,288 channels (186–1042 nm) in the recorded spectra. Wavelengths with an  $R^2$  (coefficient of determination)  $>0.7$ , suggesting a high degree of correlation with N content, were marked as candidate N lines. To avoid confusion with other elements that may have also been correlated with the N content (e.g., O in the  $\text{NO}_3^-$  ion), the flagged emission features were also required to meet the following selection criteria:

- 1) The wavelength should coincide with a reference wavelength for N emission listed in the NIST database [31].
- 2) The wavelength region should be featureless in the blank sample (Mars Global Simulant) in order to avoid false attribution of N to an emission feature associated with the matrix material.
- 3) The peak height must rise sufficiently above the level of the background emission such that it may be reliably distinguished from noise. Specifically, we only considered a candidate emission peak to be ‘detected’ as N if the peak height was  $>3\times$  the standard deviation of the random noise on the baseline measured from a featureless portion of the spectrum before or after the signal peak.

Emission features with a strong correlation with N content and met these additional criteria were considered as robust and diagnostic signatures of N, suitable for *detection* in Mars-like matrices.

### 3. Results: LIBS spectra and general characteristics

Exemplary spectra from each sample suite are shown in Fig. 1. As expected, the N lines exhibit a very weak intensity relative to the emission of other elements in the matrices, especially elements of the alkali metal, alkaline-earth metal, and transition metal groups, which dominate each spectral fingerprint. Twenty spectroscopic lines were found to be highly correlated with the known N content in the pure salt samples and satisfied the three criteria described in Section 2.3 as being diagnostic N emission features. These therefore represent the subset of *theoretical* N emission lines that are consistently *detectable* across a range of Mars-relevant  $\text{NO}_3^-$  salts. Table 3 provides a list of these lines along with comments regarding their emission behaviour, potential spectral interferences, the minimum level at which they could be reliably detected in the nitrate samples set (limit of detection), and a record of whether the lines were also observed in the spectra from the ammoniated clay sample suite.

When mixed with Mars Global Simulant (MGS-1), the spectra become much more complicated, posing challenges for the detection of N emission lines and increasing the likelihood of non-detection due to spectral interference. Specifically, only 17 of the 20 identifiable N lines could be discerned in samples that incorporated the MGS-1 simulant, with progressively fewer lines detected as the salt content declined (Table 3). We did not observe any N lines in the lowest doping condition (0.5 wt%  $\text{NO}_3^-$ ), suggesting that this is below the limit of detection achievable by our setup.

It is noteworthy to highlight the differences between our observations and previous studies on LIBS N emission for Mars applications as several N lines reported previously were not detected here, despite being within the range of our detector. First, we do not detect any of the fifteen N emission lines reported by Cousin et al. (2011) [32] in the *Laser Induced Breakdown Spectroscopy Library for the Martian Environment* (later incorporated into the *ChemCam Quick Element Search Tool* (C-QuEST)). These N signals were acquired through the ablation of pure metal targets (e.g., sheets of titanium, iron, or manganese with  $>99.98\%$  purity), whereby the N signals originated from the breakdown of the  $\text{N}_2$  present in the buffer gas of the sample chamber [32]. As a result, the reported N lines were not subject to the spectral interference or matrix effects encountered in heterogeneous geologic samples, making them less representative of the emission environment expected during in situ LIBS surveys on Mars.

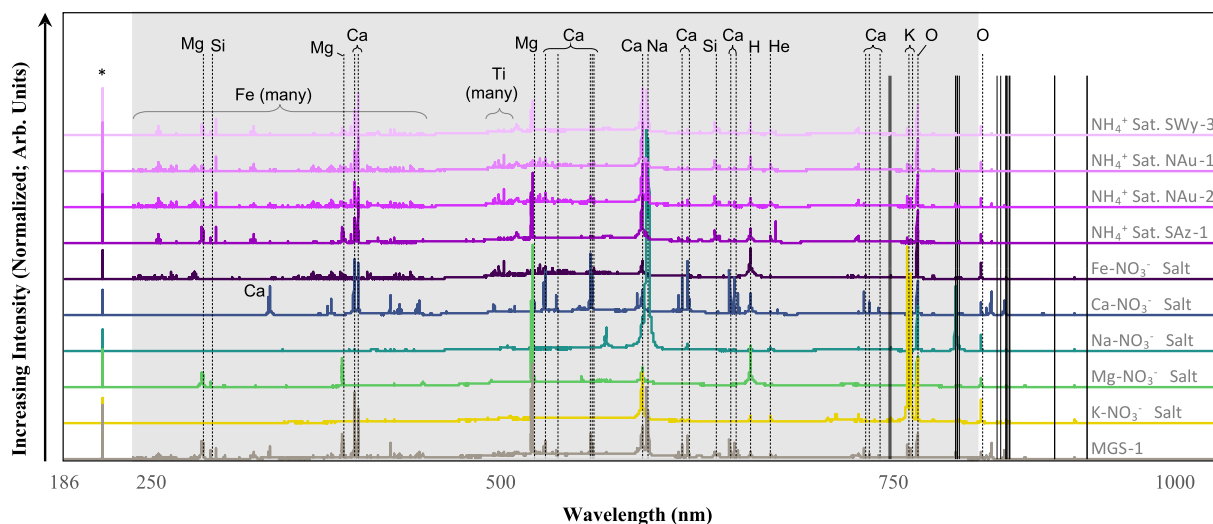


**Fig. 1.** Representative LIBS spectra from samples used in this study. The position of the N emission lines identified in this study (listed in Table 3) are marked with solid black lines. Co-occurring emission from elements of the matrix and atmosphere are marked with dashed lines and labels; identification of co-occurring elements is not exhaustive in this figure for simplicity. The grey shading marks the spectral range used by the LIBS instruments onboard the three Mars rovers active at the time of writing. The asterisks marks the 213 nm emission feature from the laser.



**Table 3**

Diagnostic N lines. These lines exhibit a high correlation with the N content of the sample and satisfy the initial three criteria listed in [section 2.3](#). Column 3 lists the lowest concentration that the given peak could be observed within the nitrate sample series – the limit of detection. Column 4 provides a record of which lines could be observed in which of the  $\text{NH}_4^+$ -bearing clay samples. Italicized rows are beyond the spectral range of the LIBS instruments currently operational on Mars.

Emission Wavelength (nm)	Comments	Lowest Concentration that a Peak is Observed in the Nitrate Dilution Series (wt%)	Peak Observed in the Ammoniated Clay Samples?
744.2	Some interference from weak Fe peak at 744.6 nm in high-Fe samples	5	Yes: N <sub>AU</sub> -1, S <sub>AZ</sub> -1, S <sub>WY</sub> -3
746.8	Strong, slight interference from unresolved grouping of O peaks at 747.6–748.6 nm	5	Yes: N <sub>AU</sub> -1, N <sub>AU</sub> -2, S <sub>AZ</sub> -1, S <sub>WY</sub> -3
818.5	Interference from Na at 818.3 nm	Pure salts only; not detected in samples with MGS-1	No
818.8	Interference from Na at 818.3 nm	15	Non
820.2	Weak; Interference from Na at 819.5 nm	Pure salts only; not detected in samples with MGS-1	No
821.6	Strong; Superimposed on Na shoulder (819.5 nm) in high-Na samples	5	Yes: N <sub>AU</sub> -1, S <sub>AZ</sub> -1, S <sub>WY</sub> -3
822.3	Weak; Superimposed on Na shoulder (819.5 nm) in high-Na samples	Pure salts only; not detected in samples with MGS-1	No
859.4	Weak	25	No
862.9	Moderate	10	No
868.0	Strong, part of a triplet emission pattern with N peaks at 868.3 and 868.6	5	Yes: N <sub>AU</sub> -1, N <sub>AU</sub> -2, S <sub>AZ</sub> -1, S <sub>WY</sub> -3
868.3	Moderate, part of a triplet emission pattern with N peaks at 868.0 and 868.6	10	No
868.6	Moderate, part of a triplet emission pattern with N peaks at 868.0 and 868.3	10	No
870.3	Moderate	10	No
871.2	Moderate	10	No
871.9	Moderate	10	No
904.6	Weak	15	No
905.0	Weak	15	No
906.0	Weak	25	No
938.7	Weak	10	No
939.3	Weak	10	No

Similarly, emission of N at 500.5 nm, described by Dequaire et al. (2017) [24] for the study of N-bearing organic molecules within lab-synthesized nontronite, failed to meet our criteria for a reliable detection. The spectral region around 500.5 nm was not free from interference in many of our samples, which impeded the clear identification of the 500.5 nm N emission. For instance, several of the cationic constituents of the pure salt phases have emission in this region (e.g., K emission at 500.56 nm, Ca emission at 500.15 nm, and multiple Fe emission lines between 500 and 501 nm [31]). Furthermore, in samples mixed with MGS-1 or clay, this portion of the spectrum was dominated by multiple overlapping emission peaks associated with Ti (MGS-1 and the clay standards used in this study contain detectable levels of  $\text{TiO}_2$ , see Table S2 in the Appendix). This latter finding is consistent with

previous work by Harris et al. [22], who demonstrated that it is not possible to construct an accurate N calibration curve in the spectral region between  $\approx 498$ –504 nm when Ti is present due to the overlapping emission features. The dominance of Ti emission in this spectral region would pose a particular challenge for detecting the 500.5 nm N line during in situ Mars application because  $\text{TiO}_2$  is a prevalent component of the bulk martian crust [33] and is distributed globally within Mars' ubiquitous dust [34]. The reason Dequaire et al. (2017) detected N at 500.5 nm is likely due to the use of a pure phase in their study, where the absence of accessory minerals limited the impact of possible spectral interferences with the N emission.

Lastly, although the theoretical N emission feature at 742.4 nm is regularly reported by other authors (e.g., [22]), especially because it forms an easily recognizable triplet pattern with the 744.2 and 746.8 nm peaks, we found that Si emission at 742.5 nm interfered with this N line in our samples. Given the resolution of our spectrometer, it was not possible to fully distinguish these two peaks in samples containing Si (present in both MGS-1 and the clay matrices) and we could not generate a linear N calibration curve using the emission feature observed near 742.4 nm. As with the Ti interference described above, spectral interferences from Si are expected to be problematic for martian application because  $\text{SiO}_2$  is a major component of Mars' crust [33]. The spectral resolution of the planetary LIBS spectrometers currently operational on Mars are insufficient to resolve these two lines (0.45 nm spectral resolution for MarSCoDe [35], 0.65 nm resolution for these wavelengths on ChemCam and SuperCam [36,37]). We therefore do not consider the 742.4 nm N line to be suitable for N detection in siliceous matrices and do not list it in [Table 3](#) as a robust N indicator.

In summary, most of the discrepancies between this study and previous work can largely be attributed to the use of different target materials, leading to variations in spectral behaviour and the presence or absence of spectral interferences. The sample suite developed for this study was designed to specifically approximate the natural geologic conditions in which fixed N is expected to occur on Mars. Consequently, the lines listed in [Table 3](#) are a catalogue of diagnostic N lines that have been validated to be detectable amid the medley of co-occurring emission lines likely to be encountered on Mars during N surveys, making them the most robust signatures for N detection during in situ analyses.

#### 4. Data processing: towards an optimal framework for quantifying N

Whereas [Table 3](#) lists the spectroscopic N lines determined to be effective for the *qualitative* detection of N in plausible Mars matrices, the remainder of this paper is focused on processing the spectra to achieve optimal *quantification* of N. Several approaches have been explored to translate LIBS spectra into quantitative element abundances. These methods can broadly be categorized as univariate and multivariate calibration schemes [48,49]. In a novel study, Dyar et al. (2016) [50] used the most extensive collection of LIBS rock spectra ever assembled, conclusively demonstrating the superior performance of multivariate calibration algorithms over univariate algorithms for geological applications. Further, they found that restricting the input data to the wavelength channels where a known emission line (or lines) from the element of interest occurs can reduce the quantification uncertainty for some minor elements (N was not included in the study).

Our work therefore aims to (1) optimize key multivariate modeling parameters for accurate N quantification, and (2) assess whether restricting the spectral input to a characteristic N line (or lines) is beneficial. We first discuss the steps taken to pre-process the spectra before inputting them into the model ([section 4.1](#)), including the selection of specific N lines for testing. A primary goal of this latter task was to identify the best N lines for quantitative modeling. Subsequently, we delve into the model architectures that we will evaluate, and the criteria used to select the preferred model ([section 4.2](#)). Finally, we critically compare the models ([section 4.3](#)) and evaluate the

generalizability of the optimal model (section 4.4). Section 5 synthesizes the entire effort to discuss the implications of applying the lessons learned to Mars.

#### 4.1. Preprocessing

##### 4.1.1. Normalization

There is no universally suitable normalization procedure to compensate for parameter variations in a LIBS plasma. Instead, different methods need to be experimentally tested to understand their impact on the observed spectral behaviour of the analyte of interest [44]. Three normalization techniques were tested here for their influence on N emission behaviour. Each technique emulates a normalization procedure routinely applied to actual LIBS data returned from the ChemCam and SuperCam instruments currently operating on Mars:

- 1) *Normalized to He* involves dividing each data point by the signal intensity of the He (I) emission line at 667.8 nm [31], derived from the He buffer gas in the sample analysis chamber. This procedure is meant to simulate the practice of normalizing LIBS spectra collected on Mars to a component of the martian atmosphere (C or O derived from gaseous CO<sub>2</sub>) to standardize for fluctuations in laser/solid coupling efficiency [38].
- 2) *Normalized to Total* involves dividing each data point by the total emission intensity integrated across the complete spectral range. This procedure is akin to the “Norm 1” technique described by Clegg et al. [39] when testing calibration schemes for ChemCam.
- 3) *Normalized to Detector* involves dividing each data point by the total emission intensity integrated across the wavelength range of the detector to which the data point corresponds. This procedure is akin to “Norm 3” described in Clegg et al. [39].

A comparison of these normalization methods and their effect on the N emission signal is integrated in the next subsection.

##### 4.1.2. Selecting the most sensitive N lines

To identify which specific region(s) of the spectrum we should focus on to optimize the multivariate calibration models, we defined three criteria (in addition to those described in section 2.3) to down-select only the most robust, stable N lines. First, from the lines presented in Table 3, we aimed to filter out any lines resulting from electronic transitions involving the ground state, as these transition states are the most severely affected by self-absorption phenomena. Such phenomena can alter the spectral line profiles and hinder quantitative determination of element abundance [40]. However, upon assessment, it was determined that no lines were filtered out based on this criterion. Second, we filtered out N lines that could not be detected across a range of concentrations. This criterion removes N lines that are unsuitable for constructing multi-point calibration curves to evaluate the reliability of the relationship between the measured signal and the N content. Priority was given to N lines that were detected across the *widest* range of concentrations, as well as those that could be resolved regardless of the host matrix (i.e., detectable in both the nitrate sample suite and the ammoniated clay sample suite).

Only four of the N emission lines listed in Table 3, namely 744.2 nm, 746.8 nm, 821.2 nm, and 868.6 nm, satisfied these initial two criteria. As indicated previously, we did not observe N lines in the lowest doping condition, 0.5 wt% and only these four emission lines were detectable in samples carrying the next lowest doping condition, 5 wt% NO<sub>3</sub><sup>−</sup> (Table 3). These lines are thus detectable across the greatest range of concentrations tested. These same four lines were the only N lines detectable in the clays treated with ammonium, which retained N at levels comparable to the 5 wt% NO<sub>3</sub><sup>−</sup> condition (Table 2). It is important to note that the emission line centered at 744.2 nm was not consistently detectable at the 5 wt% NO<sub>3</sub><sup>−</sup> condition—it only surpassed our detection threshold in ~60% of the spectral replicates of each sample in the nitrate

suite—however, because it was resolved in over half of these replicates *and* was resolvable in the ammoniated clay suite, we have chosen to include it in our assessment moving forward.

As a third and final criterion for extracting the best N emission features for quantitative modeling, we required that the intensity of the candidate emission features increase proportionally with increasing N abundance in the sample suite. This is a crucial criterion. For an emission feature to be useful for quantitation, it must respond to the analyte in a predictable manner and therefore increase monotonically with increasing concentration. The simplest way to evaluate this requirement is to draw a calibration curve where the measured signal is plotted against the analyte's known concentration across a series of samples [41]. Linearly increasing trends provide the best ability to distinguish signals across a range of concentrations, thereby improving quantification. However, we did not exclude emission lines solely based on the absence of linear trends, as any monotonically increasing trend, even if not strictly linear, could still be useful for some level of quantification.

In this paper, peak areas were used to quantify the “measured signal”, rather than the height of the peak centroid. This was done because the intensity of a LIBS emission line is typically broadened over multiple spectral channels and this method accommodates for minor imprecisions in the resolution of the spectrometer. The use of peak areas is common practice for quantitative LIBS studies of geological samples [42,43]. To compute the peak areas, the Aspen Unscrambler™ software package (Aspen Technology Inc., Version 11.0) was first used to define and subtract a local linear baseline from a small range around each selected peak. The local region to be subtracted was generally selected to include any nearby N peaks or any peaks that interfered with the peaks of interest. The only exception was for the 821.6 nm peak, which lies on the shoulder of a high-intensity Na peak; the baseline subtraction area was defined tightly around the peak to minimize the influence of Na. After baseline correction, the area of the N peak was obtained by summing the intensity values between the local minima on either side of the N peak centroid (the specific position of the minima were selected after reviewing the N peak shapes in all our spectra and replicates). In all cases, the spectral resolution of the detector was constant across the summation area. Fig. 2 offers a graphical depiction of the wavelength ranges used for local baseline correction as well as the wavelength range used for peak area summation (a numerical summary is provided in Table S4 in the Appendix).

To draw the calibration curve, the peak areas were then plotted against the molecular fraction of N in each sample (known precisely from the doping procedure or from stoichiometry in the case of the pure salt end-members). We plot against molecular fraction because the strength of LIBS emission lines depends on the number of atoms producing emission rather than the mass of these atoms (wt%). For this initial assessment of N line response, calibration curves were only generated for the spectra acquired from the nitrate sample suite. The nitrate samples are ideal for evaluating whether a candidate N line is suitable for quantification because: (i) each sample in the suite contains a precisely controlled concentration of N, whereas the clay samples contain random abundances governed by the sorption characteristics of the clay, (ii) the nitrate sample suite was designed to cover a large range of concentrations and facilitates assessment at high and low concentrations, and (iii) the sample suite provides N sourced from five distinct nitrate minerals, allowing us to investigate the influence of chemical diversity on N response.

Fig. 3 depicts representative examples of the calibration curve exercise; additional plots are provided in Fig. S2 and S3 (Appendix). Overall, the calibration curves revealed three important results. First, regarding the unnormalized data, we found that the N peak area increased proportionally with the N content in the samples (Fig. 3, top panel). This held true for each of the four N lines considered and each of the cationic mixtures. However, the *magnitude* of change in the N peak area with increasing N concentration was not uniform between cationic mixtures, resulting in different slopes for each salt series. For instance,

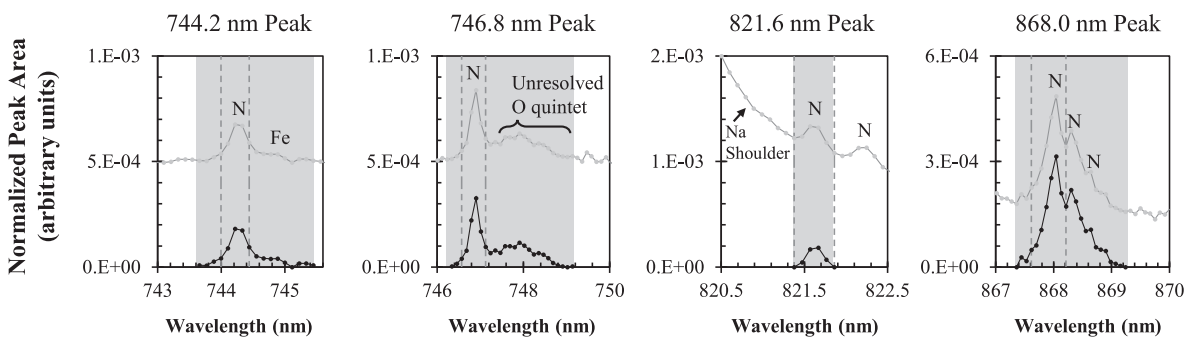


**Fig. 2.** Representative graphical depiction of the wavelength ranges used for local baseline correction and peak area summation of the four N emission features identified as potentially useful for quantification. The uncorrected spectra are depicted as a grey line. The grey shading shows the wavelength channel range used for baseline correction. Linear baseline subtraction produced spectra with 0 vertical offset, shown by the black line. The wavelength channel range used for peak area summation, following baseline subtraction, is designated by the vertical dashed lines. The position of this peak “envelope” was chosen to capture the apex of the peak and minimize interference from neighboring peaks; the specific position was based on a thorough review of our entire spectral dataset. Note, in this figure spectra have been normalized to the range of the detector.

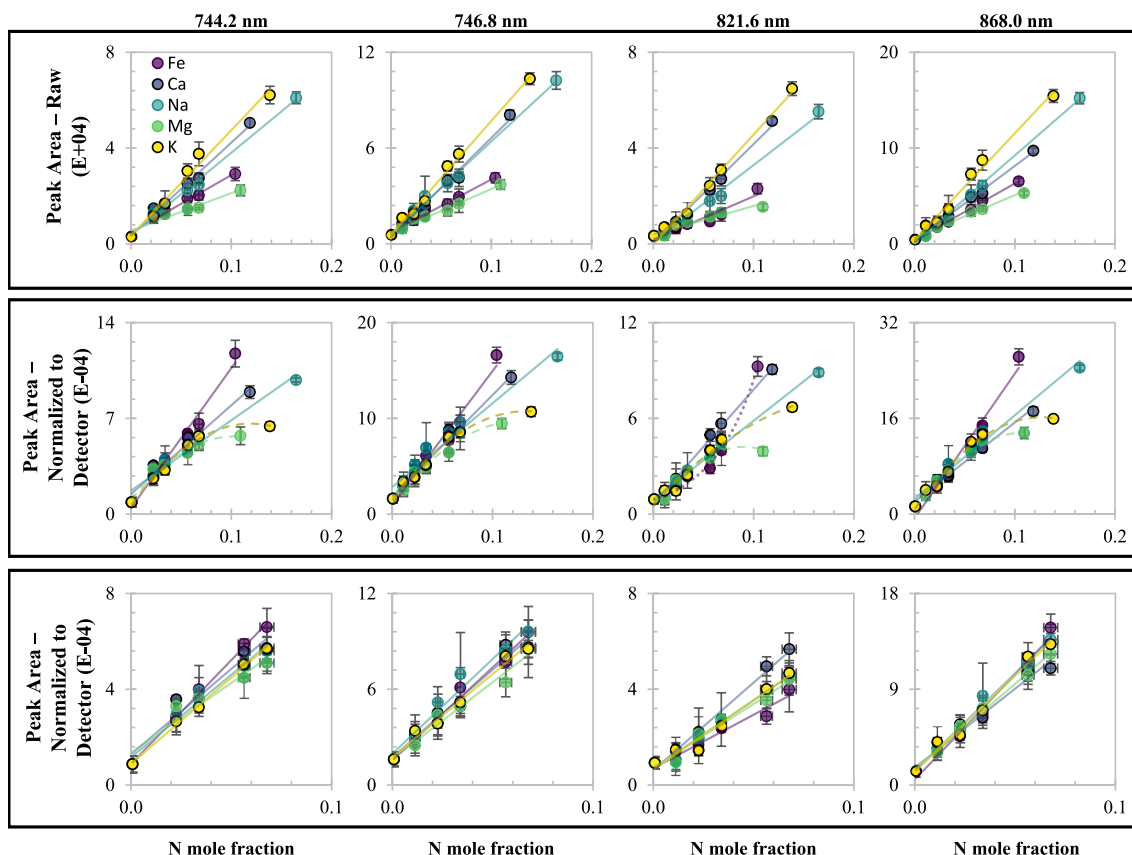


**Fig. 3.** Select calibration curves showing the measured N peak area versus the molar fraction of N. The four vertical columns correspond to the four emission lines tested (to facilitate a comparison of the usefulness of each line for tracing N concentration) and the three horizontal panels depict selected pre-processing conditions. The top panel presents the unnormalized data, showcasing the monotonic increase in measured N peak area with respect to the molecular fraction of N in the samples. The middle panel depicts the same data, but this time normalized to the total emission of the detector; additional calibration curves depicting the other tested normalization conditions are included in Fig. S2&3 (Appendix). Note the introduction of non-linear, and in some cases non-monotonic, behaviour into the relationship between the N peak area and the known N content. The bottom panel depicts the same normalized data, but with the salt endmember samples removed from the calibration curve (right-most data points). Different colours represent the different salt series, where the legend identifies the cationic composition of the salt used in the doping procedure. Each point is an average of the five replicate scans measured from each sample; vertical error bars represent the standard deviation across the five replicates. Horizontal error bars represent the average error between the calculated and validate N contents. Solid best-fit lines represent linear functions. Where a linear function lay outside 70% of the vertical error bars, an additional curve fitting algorithm was attempted: second order polynomial fits are represented by dashed lines and exponential fits are indicated by dotted lines.

the samples doped with  $\text{KNO}_3$  consistently yielded the brightest N emission peaks for each doping condition, resulting in the steepest calibration curve, whereas the samples doped with  $\text{Mg}(\text{NO}_3)_2$  yielded

the weakest peaks and shallowest slope (Fig. 3, top panel). Given that the doping procedure was designed specifically to produce samples with identical quantities of the  $\text{NO}_3^-$  ion, regardless of the salt type used during

the doping, this observation indicates that the emission behaviour of the unnormalized N emission peaks are significantly influenced by factors other than N content.

The second key observation was that all three of the normalization procedures introduced non-linear, and in some cases non-monotonic, behaviour into the relationship between the N peak area and the known N content (Fig. 3 middle panel; Fig. S2 (Appendix)). This non-linear behaviour was absent in the unnormalized data. Although a non-linear relationship between LIBS emission intensity and the analyte concentration may indicate that spectral self-absorption or detector saturation are at play [44], we reject these explanations here because: (i) our suite of selected N emission lines were filtered to avoid electronic transitions that are particularly susceptible to self-absorption, (ii) the N lines are far weaker than co-occurring cation emission lines, which themselves did not saturate the detector, (iii) we do not observe evidence of self-absorbance or saturation, such as a the characteristic distorted flat-topped peak or a peak shape with a narrow dip in the center where the strongest absorption occurs [45], and (iv) the non-linear behaviour is only apparent *after* normalizing the spectra. Furthermore, we observed that it is only the pure salt end-member samples that do not lie on the ideal linear trendline traced by the series of mixed samples (MGS-1 + salts dopant). Indeed, upon re-plotting the emission peak areas, but with the data from the pure salt end-member samples removed, the calibration curves all adopted an ideal monotonic (and linear) increasing trend (Fig. 3, bottom panel; Fig. S3 (Appendix)). Together, these observations indicate that the non-linearity observed in our calibration curves is an artefact of normalizing spectra from samples with sufficiently different matrices: pure salts and salts mixed with basalt regolith.

Consider for example, the concentration series made with KNO<sub>3</sub> salt, normalized to the total emission intensity. Potassium has a low first ionization energy (4.3 eV) and produces very bright emission lines. The pure KNO<sub>3</sub> salt spectrum is thus scaled according to a few very bright K lines, and a few relatively weak N and O lines. In samples mixed with MGS-1, the K content is diluted and the presence of other elements (from MGS-1) means that the scaling will be different. As a result, N peaks in the spectrum of pure KNO<sub>3</sub> salt will be artificially suppressed because of the strong emission intensity of K (large normalization denominator) and will not be aligned with that of the rest of the samples in the series. These findings indicate that the selected N lines respond predictably to N content in samples of similar matrices, where laser-sample interactions remain relatively constant. This suggests that normalized spectra may provide accurate calibration only within a restricted range of compositions that exhibit similar emission behaviour, but may perform poorly if extrapolated to different samples. This possibility is further evaluated in section 4.2.

The third notable result is that the *Normalization to Detector* condition equalized the calibration slopes among the different salt types to the greatest degree. This suggests that normalizing to the range of the detector most effectively corrected for the influence of the matrix on the N emission, producing a N signal that is consistently proportional to the N content, regardless of the salt type.

#### 4.1.3. Line stability

Once the characteristic lines were filtered to only those that are consistently sensitive to N content across a range of concentrations, we assessed the stability/repeatability of each line. We calculated the relative standard deviation (%RSD) of the peak areas measured across the five replicate line scans of each sample. Where,

$$\text{RSD} = \frac{\sigma}{\bar{x}} \times 100\%$$

and  $\sigma$  and  $\bar{x}$  are the standard deviation and the mean of the peak areas computed from each of the five accumulated spectra from each pellet, respectively. Higher %RSD values indicate a greater degree of spot-to-spot signal fluctuation (instability), and vice versa.

Table 4 lists the %RSD values for each of the four lines, averaged from all samples in the nitrate suite (excluding the end-member samples). Values for both normalized and unnormalized data are provided. The values range from 12.0 to 23.9% which is within the range of %RSD values previously reported from LIBS measurements of minor elements (e.g., [46,47]). A Mann–Whitney *U* test reveals no significant difference ( $p > 0.05$ ) in the emission stability of N between the normalized and unnormalized spectra. This holds true for all three tested normalization approaches and all four tested emission lines.

#### 4.2. Algorithms

Of the multivariate algorithms described in the literature, partial least squares (PLS) regression models are, by far, the most common technique applied to spectra of geological samples [50] and are the focus of this investigation. Briefly, a PLS regression model is a mathematical equation that describes the fundamental relations between two matrices (X and Y) and therefore allows a user to predict a response, Y, for a given matrix of predictors, X [51]. In the LIBS application, the X matrix is comprised of the measured LIBS data and the Y matrix is populated with reference elemental compositions.

For our work, initial PLS development was conducted only on the spectra acquired from the nitrate sample suite, for the same reasons described in section 4.1.2. These initial models were designed to optimize the input parameters for predicting N across a range of concentrations and with variable cations in the matrix (see section 4.2). As a final, additional step to assess the capacity for extrapolation, the best performing model calibrated on the nitrate sample suite was used to predict the N content of the leached and saturated NH<sub>4</sub><sup>+</sup>-bearing clay samples, which were treated as “unknowns” (see section 4.3).

We trialed three PLS permutations with different input parameters:

- 1) *Full Spectrum Model*: X matrix consisted of the entire spectral range (186–1042 nm). This model incorporates the sample's complete spectral fingerprint, including emission features from N emission lines that did not meet the feature extraction criteria described in Section 4.1.2, as well as other atoms in the sample.
- 2) *Single-Line Models*: X matrix consists of the spectral data from only one N peak. Here, a spectral range was defined around each peak (the summation window in Fig. 2) and linear baseline subtraction was applied. Then, the X matrix was populated with the individual intensity values measured across the spectral range. Separate Single-Line Models were built using spectral ranges from each peak meeting the cumulative criteria for quantification (Section 4.1.2).
- 3) *Multi-Line Models*: X matrix consists of the spectral data from multiple N peaks. This model uses the same intensity values used in model permutation 2, but the spectral ranges of each peak are concatenated into a single X matrix.

All models were developed using Aspen Unscrambler™ with the kernel PLS algorithm. Data from the complete nitrate sample suite were

**Table 4**

%RSD of selected peaks, separated by normalization treatment. Values are an average of all the %RSDs compiled for the complete nitrate suite (excluding the salt end-members), thereby representing the emission variability of these lines across a range of nitrate salt sources.

	Relative Standard Deviation of the Selected Peak Areas (%)				
	744.2 nm	746.8 nm	821.6 nm	868.0 nm	Average
Unnormalized Data	12.5	18.8	23.4	14.6	17.3
Normalized to He	12.0	19.2	23.9	17.2	18.1
Normalized to Total	13.5	18.7	23.4	18.5	18.5
Normalized to Detector	12.0	17.9	22.5	14.7	16.8
Average	12.5	18.6	23.3	16.2	



included in each model (i.e., models were not made separately for each salt type). This allowed us to assess whether the models were robust to cationic variations in salt composition and likely to be generalizable to nitrate salts not included in the study.

#### 4.2.1. Validation

Models were validated using K-fold cross validation. With K-fold cross validation, the same samples are used both for model estimation and testing. A selection of samples (a “fold”) were withheld and the model is calibrated on the remaining data points. The values of the held-out samples are then predicted using the working model and the prediction errors (residuals) are computed. The process is repeated, this time with a different fold of samples held out, and repeated again until every fold has been held out and predicted once. The prediction residuals from each iteration are then combined to compute the overall error, classically expressed as the square root of the average sum of squared errors – called the Root Mean Square Error (RMSE) of cross validation.

Here, we applied a *categorical* K-fold cross validation in which each fold contained the complete mixture series of a given salt (five folds for five different types of salts: Ca-, Na-, Fe-, Mg-, and K-nitrate). In other words, the model was trained to recognize N emission from four types of salt, variably mixed with regolith, and then used to predict the N content in the samples containing the remaining (“unknown”) salt type. By iteratively training and testing the model on the different salt series, the resultant RMSE provides an estimate of how robust the model is to predicting N from nitrate salt types that are not included in this study. It may be difficult to predict the cationic composition of a martian nitrate salt a priori, thus a calibration algorithm should be optimized such that it minimizes the prediction error across various salt types.

#### 4.2.2. Figures of merit

Two figures of merit are used here to compare the performance of the tested model permutations.  $R^2$  is a statistic that describes how well the data are fit by the regression model, where a perfect prediction would have an  $R^2$  of 1. It does not, however, indicate the accuracy of the regression model. Thus, to evaluate accuracy, we consider the RMSE. The lower the RMSE, the lower the error on the predictions achieved by the model. The RMSE has the benefit of being reported in the same units as the dependent variable. In this project, we normalize the RMSE by dividing it by the mean concentration of N in our samples, multiplied by 100. This converts the RMSE to a percentage error which facilitates comparisons between datasets or models with different scales, allowing our work to be compared with future studies that make use of different sample sets.

#### 4.3. Evaluating the performance of the PLS models: insights into an optimal quantitative N protocol

The Full Spectrum Models (model permutation 1) were built to establish a baseline. These models represent a straightforward approach to quantification, utilizing the entire spectrum without any user-defined feature selection or extraction. However, this approach was also expected to have the highest error and be the least robust due to influence from numerous other peaks in the spectra, many of which are brighter than N and are not directly relevant to the N content.

For this permutation, models were constructed using both unnormalized spectra and spectra that underwent the various normalization techniques described previously. The majority of these model iterations, with the exception of one, failed to execute successfully. Indeed, the residual variance of most of these models increased with each cross-validation step, indicating a failure to identify relevant variance in the complete LIBS spectrum for predicting N content during validation. A review of the PLS regression coefficients and variable loadings (not shown) demonstrated that the most influential variables driving the PLS predictions corresponded to emission lines from the matrix material,

such as Si, Al, Mg, Ca, Na, and K, rather than N. The resultant N predictions were so poorly fit by these models that the Aspen Unscrambler™ software failed to compute the goodness-of-fit  $R^2$  statistics. Figures of merit are thus not reported for these models, and they are taken as failures.

The only successful iteration of the Full Spectrum modeling attempt was the one based on data preprocessed with the *Normalized to Detector* condition. Despite its success, this model had significant limitations. Notably, it exhibited a high error rate (NRMSE = 45.8%), indicating a substantial deviation between predicted and actual values. Additionally, the model produced a low goodness-of-fit  $R^2$  statistic of 0.0008, demonstrating that only a very small proportion of the data's variance was explained by the model. These metrics indicate the model's poor performance and its limited capacity to accurately predict N content in the samples. Overall, the unsatisfactory results of these models underscore the inadequacy of the Full Spectrum Models in providing the requisite specificity for N quantification.

To force the models to focus on the emission trends encoded in the subtly varying N lines, permutations #2 and #3 adopt a targeted approach, exclusively using the wavelength positions validated to be sensitive to N. These permutations explore single- and multi-line calibration strategies, respectively. We repeated each Single- and Multi-Line Model on every normalized dataset, including the unnormalized data as a control, to investigate the influence of various normalizations on prediction accuracy. In addition, for each strategy, two sets of models were developed: one using the full nitrate sample suite, and the other using the restricted sample set that excluded the pure salt end-members. The rationale behind this dual construction lies in of distinct behaviour in the normalized spectra of pure end-member samples compared to those mixed with MGS-1, attributed to matrix dissimilarity (Fig. 3). Hence, a comprehensive investigation into the influence of training with limited versus broad compositional ranges was undertaken to assess its impact on the model's performance and predictive capabilities.

The exclusion of pure end-member samples yielded improvement in both prediction accuracy and regression fit for every repeated model permutation, regardless of the tested normalization (Fig. S4 (Appendix)). This finding aligns with the observations reported by Anderson et al. [52], who established that regression models trained across very different geological matrices are often inaccurate because the LIBS emission intensity of an element is influenced not only by the abundance of that element, but also by the nature of the matrix and co-existing elements. These authors demonstrated that regression models trained on a restricted range of compositions with comparable emission line behaviour can significantly improve performance within the training range. Consequently, we focused our subsequent parameter optimization investigation on the suite of models using the restricted compositional range. The performance outcomes of these models compared graphically in Fig. 4, permitting several insights to be drawn.

Firstly, we observe that normalization exerts a strong control on overall model quality. The normalized models universally exhibit superior figures of merit relative to their unnormalized counterparts. The greatest degree of improvement overall is observed in the series of models utilizing data preprocessed with the *Normalization to Detector* condition, corroborating our previous observation that this approach most effectively standardized the magnitude of the N peak areas between the sample series. Interestingly, none of the normalization methods resulted in a statistically significant change in the emission stability (%RSD) of any of the four N lines we tested (at a 95% confidence interval), indicating that normalization does not grant significant advantages in terms of the emission repeatability. The performance improvement associated with normalization is thus taken to reflect each method's capacity to standardize the N emission behaviour in different matrices (salt types), thereby producing a N signal that is consistently proportional to the N content. As above, we focus our exploration of additional parameter optimization on this subset of models normalized to the range of the detector.

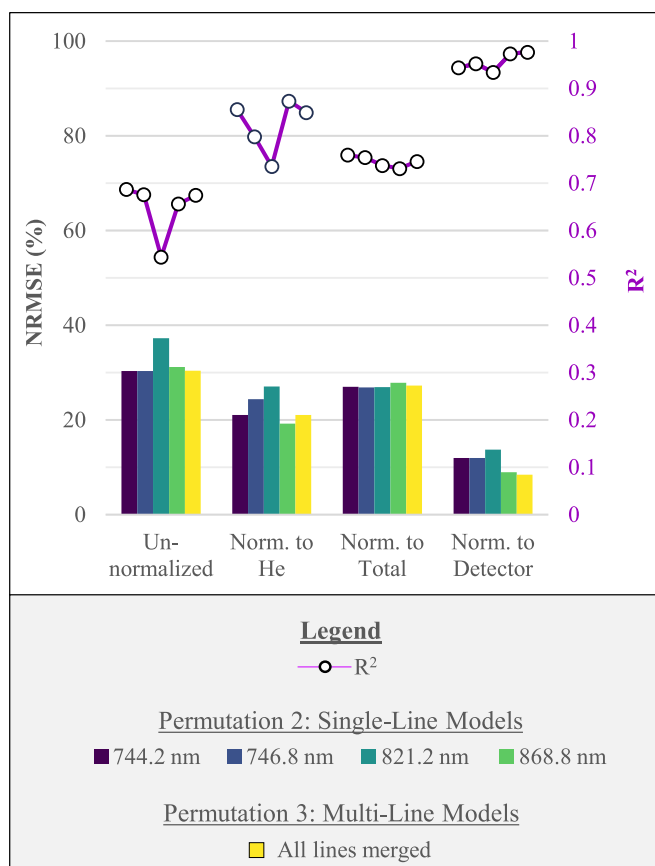


**Fig. 4.** Figures of merit for Single-Line and Multi-Line PLS models using the restricted nitrate suite after the exclusion of end-member salt samples (see text for details; a comparison with the full nitrate sample suite is available in the Appendix). Figures of merit for the Full Spectrum models could not be fully computed and are excluded from this figure. Bars depict the NRMSE (%) and are shaded according to the model permutation. Each model permutation was repeated for each normalized ("Norm.") dataset, including the unnormalized data as a control, permitting an evaluation of the relative influence of normalization on model performance. Note that the normalized datasets universally achieve lower prediction error (NRMSE) and improved model fit ( $R^2$ ), with Normalization to Detector achieving the best overall figures of merit.

Secondly, by comparing the figures of merit for each Single-Line Model within this optimal normalization framework, we can evaluate the relative efficacy of each tested N line for quantification. We find that the figures of merit are primarily influenced by the extent of spectral interference experienced by the respective N lines. For instance, the 821.6 nm N line suffers substantial interference from a bright Na peak at 819.5 nm (Fig. 2), resulting in the poorest relative figures of merit (NRMSE = 13.7% and  $R^2$  = 0.93) among the tested Single-Line Models (Fig. 4). This poor modeling outcome persisted despite the fact that the N peak was consistently detectable above the tail of the interfering Na peak and despite the tight linear baseline subtraction envelope designed to minimize Na influence (Fig. 2). In comparison, the 868.0 nm N line suffers the least interference from other emissions features in the spectrum (Fig. 2) yielding the best figures of merit (NRMSE = 9.0% and  $R^2$  = 0.97) among the tested Single-Line Models. Notably, the 868.0 nm line does not exhibit the most stable emission behaviour of the four N lines tested here, suggesting that the performance of the Single-Line Models is more significantly influenced by the absence of spectral interference than the stability of the emission lines.

Thirdly, Fig. 4 illustrates that the best overall performance is achieved by the Multi-Line Model (implemented in the *Normalization to Detector* condition), which yielded the lowest NRMSE (8.4%) and highest  $R^2$  (0.98). The regression coefficients and loadings of this model

reveal that emission in the 868.0 nm range played the most influential role as regressors. This is consistent with the relative performance of the associated Single-Line Models. However, the superior performance of the Multi-Line Model highlights the synergistic effect of combining discrete spectral ranges, resulting in an input object with predictive power that surpasses the sum of its individual parts.

As a final evaluation of PLS model optimization, we re-ran this optimal Multi-Line Model using the same spectral ranges, but without prior baseline correction for the LIBS peaks. The objective for this test was to assess the impact of baseline correction on prediction accuracy and determine if this pre-processing step was necessary. This model iteration (not shown) performed dramatically worse than the Multi-Line Model with the baseline correction applied, producing an increase in NRMSE from 8.4% to 20.2% and a decrease of  $R^2$  from 0.98 to 0.87. We suspect that this decline in performance is due to the introduction of irrelevant latent chemical information about the matrix that is encoded into the magnitude of the baseline and is uncorrelated to N content. Indeed, previous research has indicated that the LIBS baseline signal is influenced by the bulk composition of the target material, with certain elements (e.g. Mg) contributing disproportionately to the baseline shape [53,54]. The magnitude of the increase in NRMSE by simply not removing the baseline demonstrates how critical this pre-processing step is in accurately modeling subtle N variations.

#### 4.4. Evaluating the predictive accuracy in ammoniated clays

The last step in our quantification exercise was to extrapolate the best performing model, trained on the nitrate suite, to predict the N content in the ammoniated clay samples (saturated and leached conditions). Fig. 5 illustrates the result of this exercise by plotting the N content predicted by the model against the true N content, as validated by Activation Laboratories Ltd.

The predicted values consistently plot below the regression line of the calibrated model and the identity line. This suggests that our best performing nitrate-N model is biased towards consistently underestimating the ammonium-N in the clay matrices. The resulting NRMSE

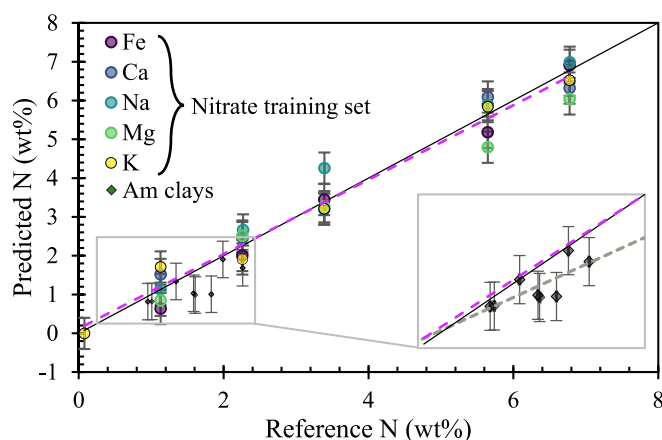


**Fig. 5.** PLS prediction model: reference N versus predicted N. The calibration model is optimized nitrate-N Multi-Line PLS model normalized to the range of the detector. Calibration data are depicted in coloured dots (the model ingested data from all the nitrate salt types simultaneously, however they are shaded distinctly in the plot to highlight that the model does not consistently over- or under-predict N based on the cationic constituent, suggesting that the model is robust to variable nitrate salt types). The calibration regression line is depicted as a purple dashed line, with the identity line in black. Grey diamonds depict the predicted N content of the ammoniated-clay samples. The inset highlights the predicted N content of the ammoniated-clay samples and the regression line of the predictions (grey dotted line). Vertical error bars are the NRMSE. (For interpretation of the references to colour in this figure legend, the reader is referred to the web version of this article.)

value of 29.9% signifies a substantial increase in uncertainty compared to the cross-validated results obtained from the nitrate samples (8.4%). Furthermore, the linear best-fit line of the predicted samples exhibits a distinct slope ( $m = 0.67$ ) that deviates from the regression line of the calibration model ( $m = 0.97$ ). This discrepancy in slope highlights that the under-prediction is not solely attributed to a linear offset (i.e., systematic under-prediction) and underscores the inadequate fit of the regression model to the predicted data. It is essential to note, however, that our confidence in this apparent under-prediction is limited by the small number of test spectra and the narrow range of N concentrations represented by the test spectra. The low N concentration range represented by the ammoniated clay samples reflects the limited capacity of the clays to uptake  $\text{NH}_4^+$ , thus, future work should focus on adding more data points to improve confidence in evaluating the model's generalizability beyond the calibration set.

## 5. Discussion: prospects for N detection and calibration on mars

The ultimate goal of this work is to enable the detection and quantification of N using LIBS during in situ exploration of Mars. However, developing quantitative calibration curves for use on Mars is beyond the scope of this project as it requires further investigation of laboratory-to-Mars instrument differences, the impact of sample distance, and the influence of the martian atmosphere on the nature of LIBS N emission. Our focus here is instead on providing a baseline understanding of LIBS N emission in Mars-relevant targets and on elucidating the generalizable strategies that improve the identification and quantification of the signal, thereby laying the foundation for these next steps. Although our work was not conducted with an apparatus or environmental conditions that truly mimic martian LIBS operation, many of our findings are independent of the acquisition conditions and may be reasonably extrapolated beyond our laboratory study to inform future planetary LIBS investigations. These are summarized below.

First and foremost, we successfully identified several emission features that are characteristic of N and consistently detectable across our range of sample compositions, reflective of the expected variations associated with the end products of N fixation on Mars. Further, we found that, despite the demonstrated effectiveness of full-spectrum LIBS multivariate algorithms for major element quantification (e.g., [39,52]), this model architecture was ineffective for discerning the subtle variations of weak N lines in Mars-like geological samples. This necessitated spectral feature extraction during the preprocessing phase. Our assessment revealed that four characteristic N lines exhibit high sensitivity to N concentration within Mars-relevant materials (744.2, 746.8, 821.6, and 868.0 nm) and we recommend these as candidate lines for constructing martian models.

While the minimum detection limit achieved with these emission lines (5 wt%  $\text{NO}_3^-$ ) exceeds the quantity of  $\text{NO}_3^-$  detected in martian materials to date ( $0.48 \pm 0.006$  wt%  $\text{NO}_3^-$  measured in Mars meteorite EETA79001 [15]), it is worth noting that Mars' reduced pressure conditions enhance LIBS plasmas, generating more intense emission signals than those observed under terrestrial conditions [44]. Our study should therefore be considered as a conservative demonstration of LIBS N detectability. Lower N concentrations may yield a resolvable signal under Mars conditions and this possibility deserves further investigation. Of course, the lower pressure conditions of Mars will also intensify signals from co-occurring and potentially interfering elements from the matrix. However, with the exception of the N emission peak at 821.6 nm which lies on the shoulder of a Na peak, the N lines discussed here are relatively free of interference and are expected to remain as robust markers of N under Mars conditions.

We found that the peak centered at 868.0 nm was the most effective regressor for N predictions (in both Single-Line and Multi-Line Models), likely because it suffered the least spectral interference from other elements. Unfortunately, the 868.0 nm line is beyond the range of the planetary LIBS instruments currently operational on Mars, which do not

detect wavelengths longer than 850 nm [35–37]. The peak centered at 746.8 nm offered the next best performance (in the Single-Line Model suite) and is within the observational range of current rovers. This therefore represents an immediately relevant emission feature with which to search for N on Mars using currently available technology. Nevertheless, we recommend that future Mars exploration missions consider an expanded LIBS range that encompasses the 868.0 nm region to optimize N detectability and quantification.

We also recommend that baseline correction and normalization be included in any future N quantification pipeline. Our findings unequivocally demonstrate that both of these techniques enhanced the model's performance, making them crucial for accurate and reliable N content predictions. However, we acknowledge that the operational conditions and hardware of planetary LIBS instruments will differ from those tested here. Consequently, although we suspect that the advantages of baseline subtraction are generalizable, we refrain from asserting the objective superiority of any specific normalization scheme. Our experiments show that normalization to the range of the detector worked best for our setup, but different conditions may yield different results. Instead, our data processing experiments should be taken as a demonstration that the thoughtful selection of a normalization procedure can enhance the accuracy and reliability of N quantification in LIBS analyses. We encourage analysts to thoroughly compare different normalization methods when operating under different conditions and emphasize that both calibration curves and PLS figures of merit can be used to rigorously determine the optimal normalization approach.

Regarding the generalization of the model, we observed that our best performing nitrate-trained model did not perform well when extrapolated to predict ammonium-derived N content in the clay sample suite. While our optimized model excelled with distinctive nitrate salts, its generalizability to all N-bearing geological samples remains limited. Our methodology does not allow us to distinguish the relative impact of the dissimilar matrices (basaltic regolith versus clay minerals) from the impact of dissimilar N sources ( $\text{NO}_3^-$  versus  $\text{NH}_4^+$ ), but our findings are consistent with previous reports that prediction accuracy declines when a regression model is extrapolated beyond the compositional range of its calibration set [55].

Future work should therefore focus on developing a diverse training set of N-bearing samples, encompassing the ranges and phases expected to be encountered on Mars. Given the limited number of N sequestration mechanisms predicted for Mars (i.e., the stabilization of  $\text{NO}_3^-$  and/or  $\text{NO}_2^-$  by regolith cations, the binding of  $\text{NH}_4^+$  on/in clays, and/or the burial of nitrogenous organic matter [5]), it is reasonable to envision the creation of a compositionally comprehensive N calibration set for Mars applications. However, both our own findings, and those of Anderson et al. [52], suggest that improved accuracy is achieved when PLS models are trained on samples with a restricted compositional range, and whose spectral line intensities respond similarly to changes in composition. Therefore, we recommend that a larger calibration set be used to develop *sub-models* optimized for specific N occurrences (e.g., nitrates dispersed in sedimentary rocks or ammoniated clays), rather than one comprehensive and generalizable model. During rover operations, contextual information from cameras (e.g., grain size), as well as chemical and mineralogical information from complementary instruments could help select the most appropriate sub-model. For instance, sedimentary rock/regolith compositions, and even specific clay minerals, may be identified by CheMin on the *Curiosity* rover [56] or by SuperCam on the *Perseverance* rover [29,57], or may be inferred through appropriate weathering proxies [58]. In addition, Hurowitz et al. (2017) [59] demonstrated that a combination of in situ mineralogy, geochemistry, textural properties, and stratigraphic relationships can be used to elucidate paleo-redox conditions, which could be helpful in predicting whether nitrogenous phases will be oxidized or reduced and selecting an appropriate sub-model.



## 6. Conclusions

The value and novelty of our works lies in the investigation of LIBS N emission from heterogeneous geologic samples specifically designed to mimic the primary end products of martian N fixation. Our investigation confirms the feasibility of detecting N using LIBS in such samples and provides key insights into reliable emission lines and relevant spectral interferences. We report 20 characteristic N emission lines that are consistently detectable in Mars-relevant nitrate salt phases, including 17 lines that are detectable when the salts are dispersed within a regolith simulant. Section 3 reveals discrepancies with several characteristic N lines reported in previous publications, attributed largely to the use of target materials that may not fully represent the expected fixed N phases on Mars. This emphasizes the importance of identifying emission features within samples closely resembling the target materials. The lines listed in Table 3 serve as a catalogue of diagnostic N lines validated to be detectable in the presence of co-occurring emission lines, making them robust signatures for N detection during *in situ* analyses on Mars.

For accurate quantification of N in our samples, we found that multivariate calibration algorithms generated from the entire LIBS spectrum lack the necessary specificity to capture N emission amidst the multitude of high-intensity lines from major rock-forming elements. Consequently, we recommend employing spectral feature extraction to focus the model on stable N emission features and enhance accuracy. Specifically, four emission lines—744.2, 746.8, 821.6, and 868.0 nm—demonstrated sufficient sensitivity to the N concentration to produce robust calibration models. The simultaneous use of all four lines for calibration modeling exhibited the best performance.

We also find that quantification accuracy is optimized by implementing baseline correction, experimentally validated normalization techniques, and restricting the calibration range to samples whose N line intensities respond similarly to changes in composition. This latter optimization yields improved performance within the restricted training range, but poor generalizability. Future work should be dedicated to developing a more comprehensive training set to encompass the range of N concentrations and phases expected to be encountered on Mars and facilitate the generation of suitably targeted sub-models.

In summary, our investigation demonstrates that LIBS holds promise as a tool for mapping astrobiologically important N in martian surface materials, despite its intrinsically weak emission characteristics. The rapid survey capabilities of LIBS uniquely position it to greatly enhance our understanding of N distribution on Mars and support our quest to decipher the planet's geological, and potentially biological, past.

## CRediT authorship contribution statement

**Erin F. Gibbons:** Conceptualization, Data curation, Formal analysis, Funding acquisition, Investigation, Methodology, Project administration, Validation, Visualization, Writing – original draft, Writing – review & editing. **Richard Léveillé:** Conceptualization, Funding acquisition, Supervision, Writing – original draft, Writing – review & editing. **Kim Berlo:** Conceptualization, Funding acquisition, Resources, Software, Supervision, Writing – original draft, Writing – review & editing.

## Declaration of competing interest

The authors declare that they have no known competing financial interests or personal relationships that could have appeared to influence the work reported in this paper.

## Data availability

Data will be made available on request.

## Acknowledgements

We acknowledge the support of the Canadian Space Agency (CSA) [21EXPCO11] and the Natural Sciences and Engineering Research Council of Canada (NSERC).

E.F.G thanks the SuperCam team for thoughtful comments, discussion, and ideas during the conceptualization and modeling stages, with special thanks to Dr. David Vogt, Dr. Sam Clegg, Dr. Roger Wiens, and Dr. Ann Ollila.

E.F.G also thanks the staff at Applied Spectra Inc. and Aspen Unscrambler for their exceptional customer support and personalized software troubleshooting.

Lastly, the authors are grateful for two anonymous reviewers whose comments greatly improved this manuscript.

## Appendix A. Supplementary data

Supplementary data to this article can be found online at <https://doi.org/10.1016/j.sab.2024.106932>.

## References

- [1] J.L. Vago, F. Westall, A.J. Coates, R. Jaumann, O. Korabely, V. Ciarletti, I. Mitrofanov, J.L. Josset, M.C. De Sanctis, J.P. Bibring, F. Rull, F. Goesmann, H. Steininger, W. Goetz, W. Brinckerhoff, C. Szopa, F. Raulin, H.G.M. Edwards, L. G. Whyte, A.G. Fairén, J. Bridges, E. Hauber, G.G. Ori, S. Werner, D. Loizeau, R. O. Kuzmin, R.M.E. Williams, J. Flahaut, F. Forget, D. Rodionov, H. Svedhem, E. Sefton-Nash, G. Kminek, L. Lorenzoni, L. Joudrier, V. Mikhailov, A. Zashchirinskiy, S. Alexashkin, F. Calantropio, A. Merlo, P. Poulakis, O. Witasse, O. Bayle, S. Bayón, U. Meierhenrich, J. Carter, J.M. García-Ruiz, P. Baglioni, A. Haldemann, A.J. Ball, A. Debus, R. Lindner, F. Haessig, D. Monteiro, R. Trautner, C. Voland, P. Rebeyre, D. Gouly, F. Didot, S. Durrant, E. Zekri, D. Koschny, A. Toni, G. Visentin, M. Zwick, M. Van Winnendael, M. Azkarate, C. Carreau, Habitability on early Mars and the search for biosignatures with the ExoMars rover, *Astrobiology* 17 (2017) 471–510, <https://doi.org/10.1089/ast.2016.1533>.
- [2] J.P. Grotzinger, J. Crisp, A.R. Vasavada, R.C. Anderson, C.J. Baker, R. Barry, D. F. Blake, P. Conrad, K.S. Edgett, B. Ferdowski, Mars science laboratory mission and science investigation, *Space Sci. Rev.* 170 (2012) 5–56.
- [3] K.A. Farley, K.H. Williford, K.M. Stack, R. Bhartia, A. Chen, M. de la Torre, K. Hand, Y. Goreva, C.D.K. Herd, R. Hueso, Mars 2020 Mission overview, *Space Sci. Rev.* 216 (2020) 1–41.
- [4] Space Studies Board and National Research Council, *An Astrobiology Strategy for the Exploration of Mars*, National Academies Press, Washington, DC, 2007.
- [5] R.L. Mancinelli, A. Banin, Where is the nitrogen on Mars? *Int. J. Astrobiol.* 2 (2003) 217–225, <https://doi.org/10.1017/S1473550403001599>.
- [6] C. Nelson, *Lehninger's Principles of Biochemistry*, 2013.
- [7] J.J. Elser, M.E.S. Bracken, E.E. Cleland, D.S. Gruner, W.S. Harpole, H. Hillebrand, J.T. Ngai, E.W. Seabloom, J.B. Shurin, J.E. Smith, Global analysis of nitrogen and phosphorus limitation of primary producers in freshwater, marine and terrestrial ecosystems, *Ecol. Lett.* 10 (2007) 1135–1142.
- [8] C.S. Cockell, Trajectories of martian habitability, *Astrobiology* 14 (2014) 182–203, <https://doi.org/10.1089/ast.2013.1106>.
- [9] A. Segura, R. Navarro-González, Nitrogen fixation on early Mars by volcanic lightning and other sources, *Geophys. Res. Lett.* 32 (2005) 1–4, <https://doi.org/10.1029/2004GL021910>.
- [10] R. Navarro-González, K.F. Navarro, P. Coll, C.P. McKay, J.C. Stern, B. Sutter, P. D. Archer, A. Buch, M. Cabane, P.G. Conrad, J.L. Eigenbrode, H.B. Franz, C. Freissinet, D.P. Glavin, J.V. Hoggan, A.C. McAdam, C.A. Malespin, F. J. Martín-Torres, D.W. Ming, R.V. Morris, B. Prats, F. Raulin, J.A. Rodríguez-Manfredi, C. Szopa, M.P. Zorzano-Mier, P.R. Mahaffy, S. Atreya, M.G. Trainer, A. R. Vasavada, Abiotic input of fixed nitrogen by bolide impacts to Gale crater during the Hesperian: insights from the Mars science laboratory, *J. Geophys. Res. Planets* 124 (2019) 94–113, <https://doi.org/10.1029/2018JE005852>.
- [11] C.V. Manning, K.J. Zahnle, C.P. McKay, Impact processing of nitrogen on early Mars, *Icarus* 199 (2009) 273–285, <https://doi.org/10.1016/j.icarus.2008.10.015>.
- [12] D.P. Summers, R.C.B. Basa, B. Khare, D. Rodoni, Abiotic nitrogen fixation on terrestrial planets: reduction of NO to ammonia by FeS, *Astrobiology* 12 (2012) 107–114, <https://doi.org/10.1089/ast.2011.0646>.
- [13] J.L. Bishop, A. Banin, R.L. Mancinelli, M.R. Klovstad, Detection of soluble and fixed NH<sub>4</sub><sup>+</sup> in clay minerals by DTA and IR reflectance spectroscopy: a potential tool for planetary surface exploration, *Planet. Space Sci.* 50 (2002) 11–19, [https://doi.org/10.1016/S0032-0633\(01\)00077-0](https://doi.org/10.1016/S0032-0633(01)00077-0).
- [14] R. Nieder, D.K. Benbi, H.W. Scherer, Fixation and defixation of ammonium in soils: a review, *Biol. Fertil. Soils* 47 (2011) 1–14, <https://doi.org/10.1007/s00374-010-0506-4>.
- [15] S.P. Kounaves, B.L. Carrier, G.D. O'Neil, S.T. Stroble, M.W. Claire, Evidence of martian perchlorate, chlorate, and nitrate in Mars meteorite EETA79001: implications for oxidants and organics, *Icarus* 229 (2014) 206–213, <https://doi.org/10.1016/j.icarus.2013.11.012>.



- [16] M. Grady, I.P. Wright, C.T. Phillinger, A search for nitrates in Martian meteorites, *J. Geophys. Res. Planets* 100 (1995) 5449–5455.
- [17] J.C. Stern, B. Sutter, R. Navarro-González, C.P. McKay, P.D.A. Jr, A. Buch, A. Brunner, J.L. Eigenbrode, A.G. Fairén, H.B. Franz, D.P. Glavin, S. Kashyap, A. C. Mcadam, W. Douglas, A. Steele, C. Szopa, J.J. Wray, F. Javier, M. Zorzano, P. G. Conrad, R. Paul, J.C. Stern, B. Sutter, C. Freissinet, R. Navarro-González, C. P. McKay, Evidence for indigenous nitrogen in sedimentary and aeolian deposits from the curiosity rover investigations at Gale crater, Mars, *Proc. Natl. Acad. Sci. U. S. A.* 112 (2015) E3085, <https://doi.org/10.1073/pnas.1507795112>.
- [18] B. Sutter, J.B. Dalton, S.A. Ewing, R. Amundson, C.P. McKay, Terrestrial analogs for interpretation of infrared spectra from the Martian surface and subsurface: sulfate, nitrate, carbonate, and phyllosilicate-bearing atacamite desert soils, *Eur. J. Vasc. Endovasc. Surg.* 112 (2007) 1–19, <https://doi.org/10.1029/2006JG000313>.
- [19] C.V. Manning, C.P. McKay, K.J. Zahnle, The nitrogen cycle on Mars: impact decomposition of near-surface nitrates as a source for a nitrogen steady state, *Icarus* 197 (2008) 60–64, <https://doi.org/10.1016/j.icarus.2008.04.015>.
- [20] S. Maurice, S.M. Clegg, R.C. Wiens, O. Gasnault, W. Rapin, O. Forni, A. Cousin, V. Sautter, N. Mangold, L. Le Deit, ChemCam activities and discoveries during the nominal mission of the Mars science laboratory in Gale crater, Mars, *J. Anal. At. Spectrom.* 31 (2016) 863–889.
- [21] R.C. Wiens, A. Udry, O. Beyssac, C. Quantin-Nataf, N. Mangold, A. Cousin, L. Mandon, T. Bosak, O. Forni, S.M. McLennan, V. Sautter, A. Brown, K. Benzerara, J.R. Johnson, L. Mayhew, S. Maurice, R.B. Anderson, S.M. Clegg, L. Crumpler, T.S. J. Gabriel, P. Gasda, J. Hall, B.H.N. Horgan, L. Kah, C. Legett IV, J.M. Madariaga, P. Y. Meslin, A.M. Ollila, F. Poulet, C. Royer, S.K. Sharma, S. Siljeström, J.I. Simon, T. E. Acosta-Maeda, C. Alvarez-Llamas, S.M. Angel, G. Arana, P. Beck, S. Bernard, T. Bertrand, B. Bousquet, K. Castro, B. Chide, E. Clavé, E. Cloutis, S. Connell, E. Dehouck, G. Dromart, W. Fischer, T. Fouchet, R. Francis, J. Frydenvang, O. Gasnault, E. Gibbons, S. Gupta, E.M. Hausrath, X. Jacob, H. Kalucha, E. Kelly, E. Knutsen, N. Lanza, J. Laserna, J. Lasue, S. Le Mouélic, R. Leveillé, G.L. Reyes, R. Lorenz, J.A. Manrique, J. Martinez-Frias, T. McConnochie, N. Melikechi, D. Mimoun, F. Montmessin, J. Moros, N. Murdoch, P. Pilleri, C. Pilorget, P. Pinet, W. Rapin, F. Rull, S. Schröder, D.L. Shuster, R.J. Smith, A.E. Stott, J. Tarnas, N. Turenne, M. Veneranda, D.S. Vogt, B.P. Weiss, P. Willis, K.M. Stack, K. H. Williford, K.A. Farley, Compositionally and density stratified igneous terrain in Jezero crater, Mars, *Sci. Adv.* 8 (2022) 1–16, <https://doi.org/10.1126/sciadv.abc3399>.
- [22] R.D. Harris, D.A. Cremers, M.H. Ebinger, B.K. Bluhm, Determination of nitrogen in sand using laser-induced breakdown spectroscopy, *Appl. Spectrosc.* 58 (2004) 770–775, <https://doi.org/10.1366/0003702041389201>.
- [23] D.W. Hahn, N. Omenetto, Laser-induced breakdown spectroscopy (LIBS), part II: review of instrumental and methodological approaches to material analysis and applications to different fields, *Appl. Spectrosc.* 66 (2012) 347–419, <https://doi.org/10.1366/11-06574>.
- [24] T. Dequaire, P.Y. Meslin, P. Beck, M. Jaber, A. Cousin, W. Rapin, J. Lasne, O. Gasnault, S. Maurice, A. Buch, C. Szopa, P. Coll, Analysis of carbon and nitrogen signatures with laser-induced breakdown spectroscopy: the quest for organics under Mars-like conditions, *Spectrochim. Acta Part B At Spectrosc.* 131 (2017) 8–17, <https://doi.org/10.1016/j.sab.2017.02.015>.
- [25] K.M. Cannon, D.T. Britt, T.M. Smith, R.F. Fritsche, D. Batchelder, Mars global simulant MGS-1: a Rocknest-based open standard for basaltic martian regolith simulants, *Icarus* 317 (2019) 470–478, <https://doi.org/10.1016/j.icarus.2018.08.019>.
- [26] G.E. Erickson, The Chilean nitrate deposits, *Am. Sci.* 71 (1983) 366–374.
- [27] F. Wang, B.B. Bowen, J.-H. Seo, G. Michalski, Laboratory and field characterization of visible to near-infrared spectral reflectance of nitrate minerals from the Atacama Desert, Chile, and implications for Mars, *Am. Mineral.* 103 (2018) 197–206.
- [28] L. Chen, S.L. Larson, J.H. Ballard, Y. Ma, Q. Zhang, J. Li, L. Wu, Z. Arslan, F.X. Han, Laboratory spiking process of soil with various uranium and other heavy metals, *MethodsX* 6 (2019) 734–739.
- [29] E. Gibbons, R. Léveillé, K. Berlo, Data fusion of laser-induced breakdown and Raman spectroscopies: enhancing clay mineral identification, *Spectrochim. Acta Part B At Spectrosc.* 170 (2020) 105905, <https://doi.org/10.1016/j.sab.2020.105905>.
- [30] B.L. Ehlmann, J.F. Mustard, S.L. Murchie, J.-P. Bibring, A. Meunier, A.A. Fraeman, Y. Langevin, Subsurface water and clay mineral formation during the early history of Mars, *Nature* 479 (2011) 53–60, <https://doi.org/10.1038/nature10582>.
- [31] A. Kramida, Yu. Ralchenko, J. Reader, NIST ASD Team, NIST Atomic Spectra Database (Version 5.6.1), National Institute of Standards and Technology, 2018, <https://doi.org/10.18434/T4W30F>.
- [32] A. Cousin, O. Forni, S. Maurice, O. Gasnault, C. Fabre, V. Sautter, R.C. Wiens, J. Mazoyer, Laser induced breakdown spectroscopy library for the Martian environment, *Spectrochim. Acta Part B At Spectrosc.* 66 (2011) 805–814, <https://doi.org/10.1016/j.sab.2011.10.004>.
- [33] S.R. Taylor, S. McLennan, *Planetary Crusts: Their Composition, Origin and Evolution*, Cambridge University Press, 2009.
- [34] J. Lasue, A. Cousin, P.Y. Meslin, N. Mangold, R.C. Wiens, G. Berger, E. Dehouck, O. Forni, W. Goetz, O. Gasnault, W. Rapin, S. Schroeder, A. Ollila, J. Johnson, S. le Mouélic, S. Maurice, R. Anderson, D. Blaney, B. Clark, S.M. Clegg, C. d'Uston, C. Fabre, N. Lanza, M.B. Madsen, J. Martin-Torres, N. Melikechi, H. Newsom, V. Sautter, M.P. Zorzano, Martian Eolian dust probed by ChemCam, *Geophys. Res. Lett.* 45 (2018) 10,968–10,977, <https://doi.org/10.1029/2018GL079210>.
- [35] W. Xu, X. Liu, Z. Yan, L. Li, Z. Zhang, Y. Kuang, H. Jiang, H. Yu, F. Yang, C. Liu, T. Wang, C. Li, Y. Jin, J. Shen, B. Wang, W. Wan, J. Chen, S. Ni, Y. Ruan, R. Xu, C. Zhang, Z. Yuan, X. Wan, Y. Yang, Z. Li, Y. Shen, D. Liu, B. Wang, R. Yuan, T. Bao, R. Shu, The MarSCoDe Instrument Suite on the Mars Rover of China's Tianwen-1 Mission, The Author(s), Under Exclusive Licence to Springer Nature B.V., 2021, <https://doi.org/10.1007/s11214-021-00836-5>.
- [36] R.C. Wiens, S. Maurice, S.H. Robinson, A.E. Nelson, P. Cais, P. Bernardi, R. T. Newell, S. Clegg, S.K. Sharma, S. Storms, J. Deming, D. Beckman, A.M. Ollila, O. Gasnault, R.B. Anderson, Y. André, S. Michael Angel, G. Arana, E. Auden, P. Beck, J. Becker, K. Benzerara, S. Bernard, O. Beyssac, L. Borges, B. Bousquet, K. Boyd, M. Caffrey, J. Carlson, K. Castro, J. Celis, B. Chide, K. Clark, E. Cloutis, E. C. Cordoba, A. Cousin, M. Dale, L. Deflores, D. Delapp, M. Deleuze, M. Dirmyer, C. Donny, G. Dromart, M. George Duran, M. Egan, J. Ervin, C. Fabre, A. Fau, W. Fischer, O. Forni, T. Fouchet, R. Fresquez, J. Frydenvang, D. Gasway, I. Gontijo, J. Grotzinger, X. Jacob, S. Jacquinet, J.R. Johnson, R.A. Klisiewicz, J. Lake, N. Lanza, J. Laserna, J. Lasue, S. le Mouélic, C. Legett, R. Leveillé, E. Lewin, G. Lopez-Reyes, R. Lorenz, E. Lorigny, S.P. Love, B. Lucero, J.M. Madariaga, M. Madsen, S. Madsen, N. Mangold, J.A. Manrique, J.P. Martinez, J. Martinez-Frias, K.P. McCabe, T.H. McConnochie, J.M. McGlown, S.M. McLennan, N. Melikechi, P.Y. Meslin, J.M. Michel, D. Mimoun, A. Misra, C. Montagnac, F. Montmessin, V. Mousset, N. Murdoch, H. Newsom, L.A. Ott, Z.R. Ousnamer, L. Pares, Y. Parot, R. Pawluczyk, C. Glenn Peterson, P. Pilleri, P. Pinet, G. Pont, F. Poulet, C. Provost, B. Quertier, H. Quinn, W. Rapin, J.M. Reess, A.H. Regan, A. L. Reyes-Nowell, P.J. Romano, C. Royer, F. Rull, B. Sandoval, J.H. Sarrao, V. Sautter, M.J. Schoppers, S. Schröder, D. Seitz, T. Shepherd, P. Sobron, B. Dubois, S. Sridhar, M.J. Topley, I. Torre-Fdez, I.A. Trettel, M. Underwood, A. Valdez, J. Valdez, D. Venhaus, P. Willis, The SuperCam Instrument Suite on the NASA Mars, 2020 Rover: Body Unit and Combined System Tests, The Author(s), 2021, <https://doi.org/10.1007/s11214-020-00777-5>.
- [37] R.C. Wiens, S. Maurice, B. Barraclough, M. Saccoccio, W.C. Barkley, J.F. Bell, S. Bender, J. Bernardin, D. Blaney, J. Blank, M. Bouyé, N. Bridges, N. Bultman, P. Cais, R.C. Clanton, B. Clark, S. Clegg, A. Cousin, D. Cremers, A. Cros, L. Deflores, D. Delapp, R. Dingle, C. D'Uston, M. Darby Dyar, T. Elliott, D. Enemark, C. Fabre, M. Flores, O. Forni, O. Gasnault, T. Hale, C. Hays, K. Herkenhoff, E. Kan, L. Kirkland, D. Kouach, D. Landis, Y. Langevin, N. Lanza, F. Larocca, J. Lasue, J. Latino, D. Limonadi, C. Lindensmith, C. Little, N. Mangold, G. Manhes, P. Mauchien, C. McKay, E. Miller, J. Mooney, R.V. Morris, L. Morrison, T. Nelson, H. Newsom, A. Ollila, M. Ott, L. Pares, R. Perez, F. Poitrasson, C. Provost, J. W. Reiter, T. Roberts, F. Romero, V. Sautter, S. Salazar, J.J. Simmonds, R. Stiglich, S. Storms, N. Striebig, J.J. Thocaven, T. Trujillo, M. Ulibarri, D. Vaniman, N. Warner, R. Waterbury, R. Whitaker, J. Witt, B. Wong-Swanson, The ChemCam instrument suite on the Mars Science Laboratory (MSL) rover: Body unit and combined system tests, *Space Sci. Rev.* 170 (2012) 167–227, <https://doi.org/10.1007/s11214-012-9902-4>.
- [38] W. Rapin, P. Meslin, S. Maurice, R.C. Wiens, D. Laporte, B. Chauviré, O. Gasnault, S. Schröder, P. Beck, S. Bender, O. Beyssac, A. Cousin, E. Dehouck, C. Drouet, O. Forni, M. Nachon, N. Melikechi, B. Rondeau, N. Mangold, N.H. Thomas, Quantification of water content by laser induced breakdown spectroscopy on Mars, *Spectrochim. Acta Part B At Spectrosc.* 130 (2017) 82–100, <https://doi.org/10.1016/j.sab.2017.02.007>.
- [39] S.M. Clegg, R.C. Wiens, R. Anderson, O. Forni, J. Frydenvang, J. Lasue, A. Cousin, V. Payré, T. Boucher, M.D. Dyar, S.M. McLennan, R.V. Morris, C.G. Graff, S. A. Mertzman, B.L. Ehlmann, I. Belgacem, H. Newsom, B.C. Clark, N. Melikechi, A. Mezzacappa, R.E. McInroy, R. Martinez, P. Gasda, O. Gasnault, S. Maurice, Recalibration of the Mars science laboratory ChemCam instrument with an expanded geochemical database, *Spectrochim. Acta Part B At Spectrosc.* 129 (2017) 64–85, <https://doi.org/10.1016/j.sab.2016.12.003>.
- [40] R. Gaudiuso, M. Dell'Aglia, O. de Pascale, G.S. Senesi, A. de Giacomo, Laser induced breakdown spectroscopy for elemental analysis in environmental, cultural heritage and space applications: a review of methods and results, *Sensors* 10 (2010) 7434–7468, <https://doi.org/10.3390/s100807434>.
- [41] J. el Haddad, L. Canioni, B. Bousquet, Good practices in LIBS analysis: review and advices, *Spectrochim. Acta Part B At Spectrosc.* 101 (2014) 171–182, <https://doi.org/10.1016/j.sab.2014.08.039>.
- [42] W. Rapin, B. Bousquet, J. Lasue, P. Meslin, J. Lacour, C. Fabre, R.C. Wiens, J. Frydenvang, Roughness effects on the hydrogen signal in laser-induced breakdown spectroscopy, *Spectrochim. Acta Part B At Spectrosc.* 137 (2017) 13–22, <https://doi.org/10.1016/j.sab.2017.09.003>.
- [43] C.R. Ytsma, M.D. Dyar, Accuracies of lithium, boron, carbon, and sulfur quantification in geological samples with laser-induced breakdown spectroscopy in Mars, Earth, and vacuum conditions, *Spectrochim. Acta Part B At Spectrosc.* 162 (2019) 105715, <https://doi.org/10.1016/j.sab.2019.105715>.
- [44] D. Cremers, L. Radziemski, *Handbook of Laser-Induced Breakdown Spectroscopy*, 2nd ed., John Wiley & Sons, Ltd, Tucson, 2013.
- [45] S.M. Aberkane, A. Safi, A. Botto, B. Campanella, S. Legnaioli, F. Poggiali, S. Ranieri, F. Rezaei, V. Palleschi, Laser-induced breakdown spectroscopy for determination of spectral fundamental parameters, *Appl. Sci. (Switzerland)* 10 (2020), <https://doi.org/10.3390/app10144973>.
- [46] C. Fabre, A. Cousin, R.C. Wiens, A. Ollila, O. Gasnault, S. Maurice, V. Sautter, O. Forni, J. Lasue, R. Tokar, D. Vaniman, N. Melikechi, In situ calibration using univariate analyses based on the onboard ChemCam targets: first prediction of Martian rock and soil compositions, *Spectrochim. Acta Part B At Spectrosc.* 99 (2014) 34–51, <https://doi.org/10.1016/j.sab.2014.03.014>.
- [47] N. Aras, Ş. Yalçın, Development and validation of a laser-induced breakdown spectroscopic method for ultra-trace determination of Cu, Mn, Cd and Pb metals in aqueous droplets after drying, *Talanta* 149 (2016) 53–61.
- [48] A.M. Ollila, H.E. Newsom, B. Clark, R.C. Wiens, A. Cousin, J.G. Blank, N. Mangold, V. Sautter, S. Maurice, S.M. Clegg, O. Gasnault, O. Forni, R. Tokar, E. Lewin, M. D. Dyar, J. Lasue, R. Anderson, S.M. McLennan, J. Bridges, D. Vaniman, N. Lanza, C. Fabre, N. Melikechi, G.M. Perrett, J.L. Campbell, P.L. King, B. Barraclough,

- D. Delapp, S. Johnstone, P.Y. Meslin, A. Rosen-Gooding, J. Williams, Trace element geochemistry (Li, Ba, Sr, and Rb) using Curiosity's ChemCam: early results for Gale crater from Bradbury landing site to Rocknest, *J. Geophys. Res. E: Planet.* 119 (2014) 255–285, <https://doi.org/10.1002/2013JE004517>.
- [49] R.B. Anderson, O. Forni, A. Cousin, R.C. Wiens, S.M. Clegg, J. Frydenvang, T.S. J. Gabriel, A. Ollila, S. Schröder, O. Beyssac, E. Gibbons, D.S. Vogt, E. Clavé, J. A. Manrique, C. Legett, P. Pilleri, R.T. Newell, J. Sarrao, S. Maurice, G. Arana, K. Benzerara, P. Bernardi, S. Bernard, B. Bousquet, A.J. Brown, C. Alvarez-Llamas, B. Chide, E. Cloutis, J. Comellas, S. Connell, E. Dehouck, D.M. Delapp, A. Essunfeld, C. Fabre, T. Fouchet, C. Garcia-Florentino, L. García-Gómez, P. Gasda, O. Gasnault, E.M. Hausrath, N.L. Lanza, J. Laserna, J. Lasue, G. Lopez, J.M. Madariaga, L. Mandon, N. Mangold, P.Y. Meslin, A.E. Nelson, H. Newsom, A.L. Reyes-Newell, S. Robinson, F. Rull, S. Sharma, J.I. Simon, P. Sobron, I.T. Fernandez, A. Udry, D. Venhaus, S.M. McLennan, R.V. Morris, B. Ehlmann, Post-landing major element quantification using SuperCam laser induced breakdown spectroscopy, *Spectrochim. Acta Part B At Spectrosc.* 188 (2022), <https://doi.org/10.1016/j.sab.2021.106347>.
- [50] M.D. Dyar, C.I. Fassett, S. Giguere, K. Lepore, S. Byrne, T. Boucher, C.J. Carey, S. Mahadevan, Comparison of univariate and multivariate models for prediction of major and minor elements from laser-induced breakdown spectra with and without masking, *Spectrochim. Acta Part B At Spectrosc.* 123 (2016) 93–104, <https://doi.org/10.1016/j.sab.2016.07.010>.
- [51] S. Wold, M. Sjöström, L. Eriksson, PLS-regression: a basic tool of chemometrics, *Chemom. Intell. Lab. Syst.* 58 (2001) 109–130, [https://doi.org/10.1016/S0169-7439\(01\)00155-1](https://doi.org/10.1016/S0169-7439(01)00155-1).
- [52] R.B. Anderson, S.M. Clegg, J. Frydenvang, R.C. Wiens, S. McLennan, R.V. Morris, B. Ehlmann, M.D. Dyar, Improved accuracy in quantitative laser-induced breakdown spectroscopy using sub-models, *Spectrochim. Acta Part B At Spectrosc.* 129 (2017) 49–57, <https://doi.org/10.1016/j.sab.2016.12.002>.
- [53] J.M. Tucker, M.D. Dyar, M.W. Schaefer, S.M. Clegg, R.C. Wiens, Optimization of laser-induced breakdown spectroscopy for rapid geochemical analysis, *Chem. Geol.* 277 (2010) 137–148, <https://doi.org/10.1016/j.chemgeo.2010.07.016>.
- [54] M.D. Dyar, S. Giguere, C.J. Carey, T. Boucher, Comparison of baseline removal methods for laser-induced breakdown spectroscopy of geological samples, *Spectrochim. Acta Part B At Spectrosc.* 126 (2016) 53–64, <https://doi.org/10.1016/j.sab.2016.10.018>.
- [55] K.H. Lepore, C.I. Fassett, E.A. Breves, S. Byrne, S. Giguere, T. Boucher, J. M. Rhodes, M. Vollinger, C.H. Anderson, R.W. Murray, M.D. Dyar, Matrix effects in quantitative analysis of laser-induced breakdown spectroscopy (LIBS) of rock powders doped with Cr, Mn, Ni, Zn, and Co, *Appl. Spectrosc.* 71 (2017) 600–626, <https://doi.org/10.1177/0003702816685095>.
- [56] M.T. Thorpe, T.F. Bristow, E.B. Rampe, N.J. Tosca, J.P. Grotzinger, K.A. Bennett, C. N. Achilles, D.F. Blake, S.J. Chipera, G. Downs, Mars science laboratory CheMin data from the Glen Torridon region and the significance of lake-groundwater interactions in interpreting mineralogy and sedimentary history, *J. Geophys. Res. Planets* 127 (2022) e2021JE007099.
- [57] E. Dehouck, O. Forni, C. Quantin-Nataf, P. Beck, N. Mangold, C. Royer, E. Clavé, O. Beyssac, J.R. Johnson, L. Mandon, Overview of the Bedrock Geochemistry and Mineralogy Observed by Supercam During Perseverance's Delta Front Campaign, in: 54th Lunar and Planetary Science Conference, 2023, p. 2862.
- [58] E. Dehouck, A. Cousin, N. Mangold, J. Frydenvang, O. Gasnault, O. Forni, W. Rapin, P.J. Gasda, G. Caravaca, G. David, Bedrock geochemistry and alteration history of the clay-bearing Glen Torridon region of Gale crater, Mars, *J. Geophys. Res. Planets* 127 (2022) e2021JE007103.
- [59] J.A. Hurowitz, J.P. Grotzinger, W.W. Fischer, S.M. McLennan, R.E. Milliken, N. Stein, A.R. Vasavada, D.F. Blake, E. Dehouck, J.L. Eigenbrode, A.G. Fairén, J. Frydenvang, R. Gellert, J.A. Grant, S. Gupta, K.E. Herkenhoff, D.W. Ming, E. B. Rampe, M.E. Schmidt, K.L. Siebach, K. Stack-Morgan, D.Y. Sumner, R.C. Wiens, Redox stratification of an ancient lake in Gale crater, Mars, *Science* (1979) 356 (2017), <https://doi.org/10.1126/science.aah6849>.